

THE EFFECT OF ADIABATIC COMPRESSION ON
THE FUNDAMENTAL PLANE OF BULGES

Chan, Jacky. Chun. Kit (ID: 20610013)

A thesis submitted for the degree of Master of
Philosophy

September 2016

STUDENT DECLARATION FORM

Concurrent registration for two or more academic awards

Either I declare that while registered as a candidate for the research degree, I have not been a registered candidate or enrolled student for another award of the University or other academic or professional institution

or I declare that while registered for the research degree, I was with the University's specific permission, a *registered candidate/*enrolled student for the following award:

Material submitted for another award

Either I declare that no material contained in the thesis has been used in any other submission for an academic award and is solely my own work

or I declare that the following material contained in the thesis formed part of a submission for the award of

(state award and awarding body and list the material below):

* delete as appropriate

Collaboration

Where a candidate's research programme is part of a collaborative project, the thesis must indicate in addition clearly the candidate's individual contribution and the extent of the collaboration. Please state below:

Signature of Candidate

J. Chan

Type of Award

MPhil Astrophysics

School

Abstract

This project has used scaling relations and the Fundamental Plane to investigate the phenomenon of bulge compression. Bulge compression takes place as disks grow around bulges. When the bulge is compressed the velocity dispersion of the bulge increases, according to the Virial theorem. This project has found the physical parameters of the uncompressed classical bulges from calculation and simulated data. This project has also found that classical bulges migrate from the scaling relations and the Fundamental Plane for elliptical galaxies during bulge compression. This can be interpreted as the morphological change of disk galaxies from being bulge-like. If a de Vaucouleurs profile can be well fitted to uncompressed bulges, then bulge compression would result in a departure from the de Vaucouleurs profile to the $n = 1$ Sérsic profile of the underlying disk. Since the uncompressed classical bulges also appear to be more elliptical, these findings have implications on our understanding of the kinematic and evolution of galaxies.

Acknowledgement

I would like to express my gratitude to my director of study Dr. V. Debattista for his unlimited guidance and support throughout the course and for this thesis. Without him I would not be able to achieve my current situation. I would also like to extend my gratitude to Dr. D .Cole and Dr. T. Cawthorne for their role in supporting my stay in this institute.

I cannot express how much I appreciate the help and guidance by my girlfriend Miss Jayne Rudd. We have managed to help each other overcoming a few unhappy episodes and as a result become stronger together. I would also like to thank Miss Anna Dunphy for her continuous friendship and support after the difficult months of early 2015, not to mention of her introducing me into 'Simon's cat'.

Gratitude also goes to Mr. Anthony Mercer and Miss Ilyena Hirskyj-Douglas. The former has assisted me through the bad times with Herr Erdinger and Mr Gordons. The latter has provided endless entertainment in forms of dogs and ridiculously cute animals found on the internet.

Last but not least thanks should go to fellow ex Royal Hollowegians Miss Abby Phillips and Miss Auguste Taruskaite. The gratitudes extended not only for their companies and friendship while I was in Royal Holloway but also for their continuous help and support through the highs and lows during my stay in Preston.

Contents

1	Introduction	3
1.1	Fundamental Plane	4
1.1.1	Redshift dependence	7
1.2	kappa space (κ -space)	8
1.2.1	Mass plane	9
1.2.2	Light plane	9
1.3	Elliptical Galaxies	10
1.4	Bulges	10
1.4.1	Bulge classification	11
1.5	Bulge formation-Pseudobulges	13
1.5.1	Disk instability	13
1.6	Bulge formation-Classical bulges	13
1.6.1	Similarity between classical bulges and elliptical galaxies	14
1.7	Bulge Compression	14
2	Sample Selection	17
3	Fundamental plane	20
3.1	Bulge decompression	20
3.2	Fundamental Plane fittings	30
3.2.1	Fundamental Plane tilting	32
3.2.2	Multi-waveband fittings	32
4	Conclusion and Summary	37

Chapter 1

Introduction

The study of galaxy formation, evolution and dynamics has fascinated professionals and laymen alike. Galaxy formation has been well studied, from the now rejected postulate of monolithic collapse to the more accepted form of hierarchical growth. With better understanding of dark matter, stellar feedback and star formation, along with more efficient simulation codes and advanced supercomputers (eg, Dirac), there have been simulations such as the Millennium simulation for galaxy formation, evolution and dynamics. This has been complemented by the advance in telescopes, such as space based telescopes (Hubble Space Telescope, Herschel), 8-meter class telescopes, adaptive optics, as well as multiwaveband observations from optical to infrared (York et al, 2000).

How does a disk galaxies evolve? This is one of the big question in the field of galaxy evolution. Does a galaxy evolve from one side of the Hubble Sequence to the other through changes in morphology? Ways to study galaxy evolution have included simulation and observations. The use of the scaling relations, such as the Fundamental Plane can also assist the analysis of galaxy evolution. The Fundamental Plane is a relation between the size, surface brightness and velocity dispersion of a galaxy. Understanding the Fundamental Plane of galaxies can establish a reliable distance indicator thus provide a glimpse of galaxy evolution (Djorgovski & Davis, 1987; Jørgensen et al, 1996).

The phenomenon of adiabatic compression for dark matter halos in galaxies was seen in simulations (Blumenthal et al, 1986). Adiabatic compression of bulges in disk galaxies has been a poorly studied topic (Andreadakis, 1998; Debattista, Kazantidis, & van den Bosch, 2013). Bulge compression was based on the assumption that some of the observed bulges and elliptical galaxies have similar morphology. The aim of this thesis is to study and test the phenomenon of bulge compression. This thesis strives to answer two questions: i) Do classical bulges experience adiabatic compression? and ii) Does bulge decompression bring

bulges closer to the scaling relations of elliptical galaxies?

This thesis is divided into the following chapters: a review of bulges, elliptical galaxies, bulge compression and the Fundamental Plane in this chapter. Data selection is detailed in chapter 2. The work and the testing of bulge compression with scaling relations and the Fundamental Plane is provided in chapter 3. The resulting conclusions are presented in chapter 4.

1.1 Fundamental Plane

For an object to be virialized it has to be in equilibrium, where the kinetic energy of the object is balanced by the gravitational potential energy of the object. One expects a relation between the velocity dispersion (σ) and the effective radius (R_e), the radius where half the light of the galaxy/bulge is enclosed. The velocity of the object is related to the mass and size via $V^2 \propto (\frac{M}{R_e})$, where V, M and R_e are the velocity, the mass and the effective radius of the object (Bernardi et al, 2003, hereafter B03). Elliptical galaxies and bulges in disk galaxies demonstrated a relation between the surface brightness of the galaxy (μ_e) and R_e , which is known as the Kormendy relation (Kormendy, 1977). A further relation between the Luminosity (L) and velocity dispersion of the galaxies is known as the Faber-Jackson relation (Faber & Jackson, 1976). The relations have provided good fits to obscured galaxies but these scaling relations still have a moderate amount of scatter. Attempts to find relations with lower scatter have found a fundamental relation incorporating R_e, σ and μ_e (the quantity L, μ_e and intensity I can be converted) (Kormendy, 1985). Fundamental Plane fitting was first carried out for early-type galaxies (Djorgovski & Davis, 1987; Dressler et al, 1987) and the Fundamental Plane has much lower intrinsic scatter compared to the Faber-Jackson and Kormendy relations. The Fundamental Plane relation can be derived through the virial theorem (Ciotti et al, 1996; Bernardi et al, 2003; D’Onofrio et al, 2006; Hyde & Bernardi, 2009) as:

$$V^2 \approx \left(\frac{M}{L}\right)R_e\left(\frac{L/2}{R_e^2}\right), \quad (1.1)$$

$$V^2 \approx \left(\frac{M}{L}\right)R_e I, \quad (1.2)$$

$$R_e \propto V^2 I^{-1}. \quad (1.3)$$

The luminosity of galaxy does not vary much (Dressler et al, 1987) thus the mass-to-light ratio (M/L) is assumed to be constant for any given galaxy thus the value of M/L is absent from eqn 1.3. Varying M/L has been explored as a factor that can affect the Fundamental Plane. When eqn 1.3 is expressed in log space it becomes:

$$\log R_e = a \log \sigma + b \log I + c, \quad (1.4)$$

where I is related to the surface brightness of the galaxy. In a perfect virial system the Fundamental Plane is known as the Virial Plane. The Virial Plane parameter has the expected value of $a = 2$ and $b = -1$ while c depends on the units utilised. The observational Fundamental Plane deviates from the virial plane, especially the value of the parameter a . The deviation from $a = 2$ is known as the tilting of the fundamental plane.

The relations between the intensity (I , with units $L_{\odot}pc^{-2}$) and surface brightness (μ , with units $mag/arcsec^2$) can be related to the surface brightness by $\mu \propto -2.5 \log I$ (D'Onofrio et al, 2006; Magoulas et al, 2012). The Fundamental Plane in log space can also take the form:

$$\log R_e = a \log \sigma + b\mu + c. \quad (1.5)$$

The value of b here differs from the value of b from eqn. 1.4. The Fundamental Plane can also be expressed in terms of the surface density of the galaxy. In this form the Fundamental Plane equation can be rewritten as:

$$\log R_e = a \log \sigma + b\Sigma + c, \quad (1.6)$$

where Σ is the surface density of the galaxy (Bolton et al, 2007). This projection of the fundamental plane has a disadvantage compared to the fundamental plane as the surface density of a galaxy is not easily obtained.

Some bulges in later-type galaxies (more likely hosting pseudobulges, Masters et al, 2011) have been found to lie at an offset from the Fundamental Plane while early-type galaxies (more likely to host classical bulges) have been found to lie close to the fundamental plane. The main difference between the two types of bulges is that classical bulges have steeper light profile while pseudobulges are flatter and have a more disk like profile. From a structural point of view classical bulges are more similar to elliptical galaxies as the classical bulges have high bulge-to-disk ratio, which means dominance of the bulge over the disk (Falc3n-Barroso et al, 2002). Simulations of elliptical galaxies have found merger remnants from bulge progenitors lie on the fundamental plane (Hjorth & Madsen, 1995).

The tilt of the Fundamental Plane has been attributed to effects such as: i) varying initial mass function (IMF), ii) varying dark matter distribution in the host galaxies, iii) deviation from homology (Capelato et al, 1995; Ciotti et al, 1996) and iv) the effect of metallicity.

IMF describes the mass distribution of stellar population in a galaxy when the galaxy forms. The IMF of the Milky Way Galaxy has been well studied, observed galaxies are assumed to have the similar IMF as the Galaxy although in reality there are differences between the IMF of the Galaxy and the IMF for different

galaxies. Dutton et al (2013) found, using the galaxies from SDSS DR7, that the residuals in the $\sigma - R_e$ relation from the Virial Plane is mass dependent. This suggested the traditional IMF is not universal. The Salpeter IMF has the tendency to overpredict (underpredict) at higher (lower) galaxy mass.

The fraction of stellar mass to total mass (M_*/M_{tot}) is not equal to one since the total mass includes all the mass within a given radius while M_* includes only the luminous matter.

Deviation from homology also contribute to the fundamental plane tilting (Graham and Colless, 1997). The de Vaucouleurs profile provides adequate surface brightness/ intensity fittings for elliptical galaxies and bulges. Some bulges deviate from the $I \approx \exp(-R^{\frac{1}{4}})$ approximation. The deviation from the profile can overestimate or underestimate the radius of the bulge/galaxy. This introduce uncertainty to the value of R_e and affects the fitting of the Fundamental Plane. Sérsic profile ($I \approx \exp(-R^{\frac{1}{n}})$) is similar to the de Vaucouleurs profile except it employs a parameter n instead of four thus allowing greater freedom when fitting the light profile.

Observations in different wavelength can also affects the Fundamental Plane fitting. The value of M/L in the near-infrared observations has been found to have large scatter compare to M/L in optical wavebands. Metallicity effect is negligible compared to other effects(Dressler et al, 1987; Pahre et al, 1995). Further hypotheses have suggested that the tilting might also originate from the velocity anisotropy, as lower velocity dispersion tends to favour a lower value for the Fundamental Plane parameter a (Hyde & Bernardi, 2009). The velocity dispersion are chosen to calculate the virial mass enclosed in the given radius, thus limit the luminosity within such radius. This also affects the measurement of M/L of the galaxy. Observations in optical wavebands have found the value M/L increases along with the metallicity although this trend is not seen in the infrared observations.

Fundamental plane tilting can be contributed by multiple effects (Prugniel & Simien, 1997) and the contribution of each effect has been debated. One study found the combination of nonhomology of the galaxies and stellar population, with a 3:1 ratio on the tilting of the Fundamental Plane (Trujillo et al, 2014). The dependency of the wavelength for the Fundamental Plane tilts can be seen in both optical and infrared (Fernández Lorenzo et al, 2011; D’Onofrio et al, 2013). In the optical wavebands the value of a varies from 1.14 in the V-band (551nm) to 1.49 in R-band (658nm) while in the infrared wavebands the value of a suffers less deviation, with the value of 1.55 in I-band (806nm) and 1.66 in K-band (2190nm) (Pahre et al, 1995; D’Onofrio et al, 2006; Hyde & Bernardi, 2009). This trend has been observed in the SDSS survey from SDSS g-band (475nm) to SDSS z-band (905nm) (Saulder et al, 2013). This finding suggests the Fundamental Plane suffers from less tilting at longer wavelength (Saulder et al, 2013), which are less prone to absorption by dust. The reason to study the Fundamental Plane in the infrared waveband is that it has a tighter relation due to less absorption (Pahre et al, 1995). Observations in infrared wavebands are not strongly affected by

dust, age or metallicity yet tilting still happen, suggesting the tilt of the Fundamental Plane maybe due to nonhomology instead (Pahre et al, 1995).

The scatter of the Fundamental Plane is also mass dependent. there is greater scatter for low mass galaxies and less scatter for the high mass galaxies thus the high mass galaxies have thinner Fundamental Plane compared to the lower mass counterpart, resulting in a curved fundamental plane. The result provided support to the idea of a composite Fundamental Plane (Hyde & Bernardi, 2009).

One of the early studies consisted of about 200 galaxies in nearby clusters but since then sample sizes have increased. Later surveys such as SDSS and 6dfGS (Magoulas et al, 2012) have larger sample in the tens of thousands. These studies studied the Fundamental Plane at different redshifts, environments, morphologies and the mechanism responsible for the Fundamental Plane tilting.

1.1.1 Redshift dependence

Local galaxies have been surveyed in detail by the Sloan Digital Sky Survey (SDSS). The SDSS Data Release 7 contains data on over 1.2 million galaxies (Abazajian et al, 2009). Studies of the Fundamental Plane have been carried out for galaxies up to $z = 2$. There were fewer galaxies in the higher redshift studies and the Fundamental Plane of these galaxies had greater scatter (van Dokkum and Stanford, 2003; van de Sande et al, 2014). These studies have provided invaluable knowledge on the evolution of the fundamental plane. The evolution of the Fundamental Plane can provide not only a distance indicator, but also to the study of the formation and evolution of galaxies (Djorgovski & Davis, 1987). The high redshift Fundamental Plane tends to suffer from sample selection biases as brighter galaxies are more likely selected in magnitude limited survey. This is one of the biggest problems with high redshift studies (van de Sande et al, 2014). The surface brightness of the galaxies observed appear diminished compare to galaxies of same size. As a result brighter galaxies were preferentially selected in magnitude limited surveys. These brighter galaxies might also be larger than the faint counterparts, as predicted by the Kormendy relation. There are fewer galaxies in higher redshift Fundamental Plane fitting as galaxies observed as late-type disk galaxies now might have evolved to early-type galaxies since then, further suggested bias towards older galaxies which formed at higher redshift (van Dokkum & Franx, 1996).

Evolution of the Fundamental Plane has been debated as surveys at low to medium redshifts suggest the effect of evolution is small (Capelato et al, 1995; B03; Herbert et al, 2011) while surveys at high redshift ($z = 1.27$) found, assuming there is no evolution in the value of a and b , strong evolution in the Fundamental Plane zero point c (van de Sande et al, 2014). There is also a noticeable evolution of M/L in the study of

massive early-type galaxies ($\ln M/L \propto (-1.06 \pm 0.09)z$) (van Dokkum and Stanford, 2003). The evolution of the zero point offset could be observational bias mimicking evolution (D’Onofrio et al, 2013).

Another postulation suggested the Fundamental Plane is merely three parameters happen to share scaling relations with an additional parameter such as redshift or blackhole mass (Fraix-Burnet, 2011).

Fraix-Burnet et al (2010) suggested that the Fundamental Plane is not made up of one plane of uniform thickness, but instead the Fundametnal Plane is composed of smaller segments of planes. This composite plane incorporates the existing Fundamental Plane parameter with an additional parameter- the Mg_2 line (Fraix-Burnet et al, 2010). The strength of the Mg_2 lines measures the α -enhancement from Type II supernovae and correlate the age of a galaxy. Around 500 galaxies from 56 clusters were separated into seven groups according to the Fundamental Plane data and the strength of the Mg_2 line. The galaxies in each of the clusters have similar size, metallicity, surface brightness and location in the clusters thus suggesting these galaxies would have similar formation mechanism.

1.2 kappa space (κ -space)

The Fundamental Plane provides a tight, low scatter, three parameter fit. The three-dimensional Fundamental Plane has the disadvantage that it is affected by the viewing angle of the Fundamental Plane. Early studies have predominately investigated the edge-on view of the plane, while later studies had attempted to find other views of the fundamental plane such as the edge-on and the face-on view of the plane (Jørgensen et al, 1996). The κ -space composed of three parameters, each depending on the parameter R_e, σ and intensity I_e (instead of μ) (Bender et al, 1992; Ciotti et al, 1996) with the form:

$$\kappa_1 = (\log \sigma^2 + \log R_e)/\sqrt{2} \quad (1.7)$$

$$\kappa_2 = (\log \sigma^2 + 2 \log I_e - \log R_e)/\sqrt{6} \quad (1.8)$$

$$\kappa_3 = (\log \sigma^2 - \log I_e - \log R_e)/\sqrt{3}. \quad (1.9)$$

Each axis corresponds to the properties of the bulge/elliptical galaxy, where $\kappa_1 \propto M$, $\kappa_2 \propto \frac{M}{L}L^3$ and $\kappa_3 \propto (M/L)$. The value of M in M/L is the dynamical mass, which includes both the stellar mass and dark matter mass (Bender et al, 1992, hereafter BBF; Gadotti, 2009, hereafter G09).

The κ -space Fundamental Plane presents an edge-on view of the Fundamental Plane in the $\kappa_3 - \kappa_1$ plane while the $\kappa_2 - \kappa_1$ plane presents the face-on view. An example can be seen from the original κ -space plane paper by BBF. The tilting of the Fundamental Plane manifests in the κ -space via the increase in the value of

κ_3 (Ciotti et al, 1996). The face-on view of the plane has provided more information on the formation history of ellipticals. The location of galaxies on the $\kappa_2 - \kappa_1$ plane provides information on the processes which the object has undergone, such as tidal stripping, ram-pressure stripping, mergers and secular evolution (see fig 2. of BBF). The $\kappa_2 - \kappa_1$ relation represents a mass and light relation. The straight line on the $\kappa_2 - \kappa_1$ plane denotes the limit of where hot stellar systems cease to exist ($\kappa_2 + \kappa_1 = 8$) (BBF). The choice of E/S0 galaxies in surveys has suggested it is more likely to include classical bulges rather than pseudobulges. The classical bulges and the elliptical galaxies have been found to be located towards the regions where mergers take place.

1.2.1 Mass plane

Another projection of the Fundamental Plane is the Mass Plane (Cappellari et al, 2013). The Mass Plane contains three parameters but instead of using the surface brightness of the bulge/galaxy, the mass is chosen instead. The mass of the object can be obtained by the Jeans equation for mass within a given radius. In the logarithmic space this plane takes the form :

$$\log M = a \log \sigma + b \log R_e + c. \quad (1.10)$$

Eqn 1.10 is a rearrangement of the virial theorem thus the Mass Plane in the virial state would have the expected value of $a = 2$ and $b = 1$. The Mass Plane has the advantage of not using luminosity, which contributes to most of the scatter in the Fundamental Plane (Cappellari et al, 2013).

1.2.2 Light plane

The light plane is another Fundamental Plane derived from the virial theorem which can be used to trace the luminosity in galaxies. The equation has the form:

$$V^2 \propto \frac{M}{L} L \frac{1}{R}, \quad (1.11)$$

$$L \frac{M}{L} \propto V^2 R, \quad (1.12)$$

where the value of M/L can vary during the lifetime of galaxies but when they are observed the value is assumed to be constant for all galaxies. Eqn. 1.12 in logarithmic form becomes:

$$\log L = a \log \sigma + b \log R_e + c. \quad (1.13)$$

Previous study has found $a = 0.7$ and $b = 1.3$ (Díaz & Muriel, 2005) for nearby galaxies. These galaxies have been chosen from the SDSS DR 3 survey as they reside in groups or cluster environments. The luminosity of galaxies was found to vary with mass and the value of M/L in this dataset also vary with mass ($M/L \propto M^{0.36}$).

1.3 Elliptical Galaxies

Elliptical galaxies are some of the oldest, largest and brightest stellar systems. The formation of elliptical galaxies was studied via simulations (Boylan-Kolchin, Ma & Quataert, 2005). Elliptical galaxies are the product of violent mergers between two progenitors, occasionally undergoing more than one merger.

The two dark matter haloes come into contact, merge and form one combined dark matter halo. The energy and angular momentum of the two galaxies' orbits contribute to the final morphology and dynamics of the merger remnants (Boylan-Kolchin, Ma & Quataert, 2005). Major mergers have been associated with the formation of elliptical galaxies, two galaxies of similar size orbiting around a pericenter, where the smaller galaxy behaves like a satellite and eventually spirals into the centre to merge with the larger of the two galaxies.

1.4 Bulges

Early observations have assumed galaxies as a single component structure where the intensity of bright elliptical galaxies can be described by the de Vaucouleurs profile ($I \propto \exp\left(\frac{R}{R_e}\right)^{-\frac{1}{4}}$), where I is the intensity function of the object enclosed within given radius (R) (de Vaucouleur, 1948)). The use of the de Vaucouleurs profile has since been found to be inadequate for all forms of galaxies. The single profile has failed to account for the excess light found near the centre of galaxies. The excess light suggests the existence of substructures within the galaxy such as a nuclear star cluster, bulges, bars, nuclear bars and nuclear disks. Two component light profiles have been found to describe the galaxy better than a single component light profile. The use of an exponential and a power law for disk galaxy light profile fittings has shown two distinct features- the disk and bulge (Andreadakis & Sanders, 1994). The outer part of the galaxy is best fitted with an almost exponential profile and a steeper slope has been fitted for the central few kiloparsec of the galaxy. Further studies of disk galaxy light profiles have found in some cases the centre portion of the galaxy deviates from the de Vaucouleurs profile (Hjorth & Madsen, 1995; Graham and Colless, 1997). The Vaucouleurs profile

overpredicts the effective radius of the object if the galaxy has the Sérsic index $n < 4$ and underpredicts the effective radius of the objects with $n > 4$. A more general profile, the Sérsic profile has been used instead. This profile has the form $I \propto \exp\left(\frac{R}{R_e}\right)^{-\frac{1}{n}}$, where n is the Sérsic index of the object. When $n = 4$ the Sérsic profile is the same as the de Vaucouleurs profile.

Bulges have been found to be more enriched and older than disks which appear younger with a shallower metallicity gradient (Kormendy & Kennicutt, 2004). Simulations found the properties at the outer part of the bulge should be similar to the inner part of the disk. The age difference between the bulge and the disk fits into the current scenarios that in a disk galaxy the bulge forms prior to the disk- the 'inside out' formation scenario (van den Bosch, 1998).

1.4.1 Bulge classification

At first glance all bulges appear similar. Some of the disk galaxies are offset from the Kormendy and Faber Jackson relations when compared with elliptical galaxies. These disk galaxies appear to be dimmer on the Kormendy relation.

Analysing the structure of disk galaxies depends on the viewing angle of the galaxies. For edge-on galaxies the difference between the best fit profile with the sample light profile can reveal substructure while two dimensional contour plots of surface brightness isophotes are best for face-on galaxies, showing features such as bars. These methods have led to the identification of increased amount of galaxies and improved classification accuracy. Human eyes might be better at identifying patterns than computers it can be subject to human error. The use of computer programs can be more time efficient and the programs can flag out galaxies with low confidence for visual inspection. The choice of programs can also play a part as most general decomposition programs only incorporate a disk+bulge model while the disk+bulge+bar model is less used (Gadotti, 2009). The exclusion of bars would ignore the bars' contribution to the luminosity of the galaxy and result in less accurate photometric information on the galaxy.

Citizen science, such as that of Galaxy Zoo (Lintott et al, 2011), has increased the number of galaxies identified by combining computer programs and visual inspection. The participants might not be experts but thanks to the stringent criteria classifications would only sustain if they are agreed amongst large numbers of volunteers.

Bulges can be separated into classical bulges and pseudobulges. Morphologically the former resembles a scaled down elliptical galaxy while the latter resembles that of a puffed up disk. The types of bulge residing in disk galaxies depends on the Hubble type of the host galaxy. Classical bulges tend to reside in early-type

galaxies while pseudobulges are found in late type galaxies (Kormendy & Kennicutt, 2004). Classification of bulges is based on a number of criteria. Some of the criteria include:

i) Sérsic index: This is one of the most used criteria as the light profile of the bulge provides tell-tale sign of the bulge type. In the sample of Gadotti (2009) (hereafter G09) there was some overlap between the classical bulges and pseudobulges but the confusion is small. Classical bulges have a steeper light profile best fitted by a Sérsic profile with $n > 2$ while pseudobulges have a more disk-like profile with $1 < n < 2$ (Fisher & Drory, 2008; Fisher & Drory, 2010, hereafter FD10)

ii) Bulge-to-Total ratio (B/T): Pseudobulges tend to reside in disk-dominated galaxies with lower value of B/T ($0.2 < B/T < 0.5$) while classical bulges reside in bulge-dominated galaxies with $B/T > 0.5$. The host galaxy of the former tends to be disk-dominated while the latter tends to be bulge-dominated.

iii) Structure: Classical bulges have smooth appearance while pseudobulges may contain internal structures such as bars, rings, dust and gas.

iv) Rotation: Rotation speed can determine the bulge type. Pseudobulges tend to have lower velocity dispersion and classical bulges have higher velocity dispersion. The ratio between the velocity dispersion and the circular velocity of the bulge (v_{cir}/σ) can also determine bulge type. If $v_{cir}/\sigma \gg 1$ then the object is flattened and is rotationally supported while an object with $v_{cir}/\sigma \approx 1$ it is isotropic and supported by the rotation and dispersion of the stars (Kormendy & Kennicutt, 2004). Velocity plateaus and velocity drops have been observed in the centre of galaxies hosting active and inactive pseudobulges (see v). These phenomena are only observed in pseudobulges but not classical bulges (Mollá & Ferrini, 1995; Méndez-Abreu et al, 2014).

v) Star formation rate (SFR): SFR of classical bulges is low compared to pseudobulges, the latter have varied SFRs. Bulges with internal structure have higher SFR (Fisher & Drory, 2010). The SFR of the pseudobulges can further identify the two subclasses of pseudobulges. Observations by Spitzer at $24\mu m$ have found some pseudobulges are still actively forming stars and observations at $3.6\mu m$ and $8\mu m$ have found that pseudobulges can further separate to active and inactive pseudobulge. Inactive pseudobulges are similar in size to the active pseudobulges but they have lower surface brightness and lower Sérsic index compared to the active pseudobulges.

vi) Scaling Relations: The Faber-Jackson relation describing the luminosity-velocity dispersion relation and the Kormendy relation describing the surface brightness-effective radius relation for elliptical galaxies is shared by the classical bulges while pseudobulges are offset from these relations. G09 postulated the Kormendy relation for galaxies with $n > 2$ and $n < 2$ (G09). Most of the bulges classified as classical bulges with $n > 2$ reside on the Kormendy relation while pseudobulges are offset below the classical bulges.

1.5 Bulge formation-Pseudobulges

The formation of pseudobulges depends on the evolution of the host disk. N-body and Smoothed Particle Hydrodynamical (SPH) simulations have provided models of the formation of pseudobulges using disk instabilities and starbursts at high redshift.

1.5.1 Disk instability

One pseudobulge formation mechanism is through disk instabilities. The duration depends on the system's energy exchange efficiency and the efficiency depends on the density and pressure of the gas, the velocity of the gas and the cloud dissipation efficiency (η) (Immeli et al, 2004, hereafter I04). The factor η is the collision cross section between clouds which depends on the magnetic field, self gravity and nature of the cloud medium. The value of η determines the cooling rate of the gas; in turn affects star formation rate thus determines the enrichment of the bulge. I04 carried out a series of galaxy formation simulations with various values of η to form disk galaxies. Different types of disk galaxies formed in the simulations, hosting different form of bulges. The mechanism of disk instability initiates when gas falls towards the disk. Due to angular momentum the gas seldom sinks to the centre. The thickness of the disk depends on the value of η , where high cooling rate results in a thinner disk. Eventually the gas settles onto the disk and become rotationally supported, leads to the disk fragmenting into stellar and gas clumps. The clumps spiral towards the centre, and merge to form high gas density environments, allowing high star formation rates and enrichment.

Other studies have found alternative pseudobulge formation mechanisms, such as high redshift starbursts (Okamoto, 2013) and formation through dynamical processes such as bar dissolution (Guedes et al, 2013).

1.6 Bulge formation-Classical bulges

Gravitational collapse was a popular formation mechanism for galaxies in the early study of galaxy formation (Eggen et al, 1962) although it has since been superseded by other ideas. Classical bulges form via quick and violent merger(s) of two between two similarly sized galaxies disk galaxies (Mo, van den Bosch & White, 2011). During the merger the two central bulges merge and the two disks merge as well, driving gas to higher density, inducing further star formation.

The merger scenario has one shortfall. It has failed to reconcile the major merger rate of the galaxies at high redshift to simulations (Kormendy & Kennicutt, 2004; Ceverino et al, 2015).

1.6.1 Similarity between classical bulges and elliptical galaxies

The morphology of a classical bulge is similar to an elliptical galaxy to be similar types of objects (G09). The radial profile of classical bulges and elliptical galaxies can both be described reasonably well by a de Vaucouleurs profile. The two also share similar kinematics and stellar populations. They also share similar scaling relations, such as the Faber-Jackson and Kormendy relations (Kormendy & Kennicutt, 2004). The Fundamental Plane of around twenty disk galaxies has found that disk dominated galaxies are at an offset from the fundamental plane while bulge dominated galaxies follow the same relations as elliptical galaxies (Falcón-Barroso et al, 2002). The offset might be due to the effect of disk dominance over bulge in the disk galaxies (Falcón-Barroso et al, 2002). Cheung et al (2013) have found, from simulations, that bar formation tends to start after the formation of classical bulges so the bars have no effect on the formation of classical bulge, while the formation of pseudobulges can only be initiated by infalling material into the centre through bars or spirals.

1.7 Bulge Compression

Bulges reside in disk galaxies at all redshifts (Djorgovski & Davis, 1987; B03; Magoulas et al, 2012). Adiabatic compression has been known in galaxies where the surrounding dark matter haloes undergo compression due to baryonic infall (Blumenthal et al, 1986; Jesset, Naab & Barkert, 2002; Cardone & Sereno, 2005; Sellwood & McGaugh, 2005). If the process of adiabatic compression does take place in galactic bulges then this provides support to the formation mechanism of bulges and further supports the idea of the bulge forms prior to the disk (inside out formation).

This thesis focuses on the properties of the central bulge during the (re)formation of the disk around the bulge, assuming a classical bulge exists in an isolated host galaxy. Previous studies postulated the phenomenon of bulge compression (Andreadakis, 1998). Both Andreadakis (1998) and Debattista, Kazantidis, & van den Bosch (2013) (hereafter D13) attempted to treat the bulge as a merger remnant and they allowed the bulge to evolve from formation to the present. There would be no new star formation episode thus the bulge mass would be the mass of the merger remnant. The lack of new star formation simplifies the problem as it keeps the stellar mass and luminosity of the formed bulge constant, any effect must come from compression of the bulge by disk growth (D13).

The studies simulated the phenomenon of bulge compression in isolated disk galaxies and compared the parameters of the bulges before and after disk growth. The final light profile of the bulge were fitted to obtain the bulge Sérsic index (Andreadakis, 1998). The Sérsic index of the bulge decreases as the bulge is

compressed. The effect of compression depends on the Sérsic index of the protobulges: the higher the initial Sérsic index, the greater decrease in Sérsic index at the end of the simulation. The study by Andreadakis (1998) provided limited scope on the effect of bulge compression as some of the classical bulges have higher Sérsic index and value of D/B than the values covered by the simulations. The phenomenon of bulge compression occurs in classical bulges rather than in pseudobulges. Morphologically the bulge does not change and the Sérsic index does not decrease lower than $n = 2$ (Andreadakis, 1998). There has little signs of bulge compression if the protobulge has $n < 2$. Another reason to study bulge compression is that SMBHs are postulated to grow in mass during compression in order to stay on the $M_{\bullet} - \sigma$ relation (Ferrarese & Merritt, 2000), where M_{\bullet} is the mass of the supermassive blackhole. A later study of $M_{\bullet} - \sigma$ relation offset suggested the offset from the relation might be due to the inclusion of barred galaxies (Hartmann et al, 2014). Bulge compression increases the velocity dispersion of the bulge, therefore the SMBHs must grow during the compression in order to stay on the $M_{\bullet} - \sigma$ relation (D13). SMBHs was found to grow by 50- 65 % during compression (D13). The simulations of bulge decompression by D13 used protobulges with $n = 4$, with various disk-to-bulge ratios. This study has observed the effect of disk growth and the changes in the physical quantities such as the velocity dispersion of the bulge and the effective radius of the bulge. The mass of the bulge (M_b) is constant, while the disk mass (M_d) is growing.

Utilising the $M_{\bullet} - \sigma$ relation can predict the growth of M_{\bullet} during compression for large number of galaxies. The ratio of the velocity dispersion before and after bulge compression yields the SMBH growth factor F, assuming a SMBH does exist in the galaxy. The gradient of the $M_{\bullet} - \sigma$ relation provides the mass of the SMBH at the time of bulge formation. The ratio of the velocity dispersion has the form of:

$$\left(\frac{\sigma_f}{\sigma_i}\right)^2 = \left(\frac{M_{b,f} + M_d}{M_{b,i}}\right) \left(\frac{R_i}{R_f}\right), \quad (1.14)$$

where f and i are the final and initial state of the system. Eqn. 1.14 is a rearrangement of the virial theorem. The effective radius of the bulge has been assumed to be the same throughout, which is not the most realistic assumption as seen in table 1 of D13. For a pressure supported system, Wolf et al (2010) found the half mass of the system can be described by:

$$M_{1/2} \simeq 4G^{-1}R_e \langle \sigma_{los}^2 \rangle \quad (1.15)$$

where σ_{los} is the line-of-sight velocity dispersion of the object. D13 computed the growth factor:

$$F = \frac{\sigma}{\sigma_0} = \left(1 + 2\gamma \left[1 - \left(1 + \frac{R_e}{R_d}\right) \exp^{-\frac{R_d}{R_e} \frac{D}{B}}\right]\right)^{\delta}, \quad (1.16)$$

where 0 denotes the initial uncompressed state of the quantity, and γ compensates for the assumption that the vertical height of the bulge is much smaller than the effective radius of the bulge. There is an additional assumption of $R_e = R_{e,0}$; the free parameter δ is related to the actual ratio $R_e/R_{e,0}$. At $R_e/R_{e,0} = 1$ the value of δ is 0.5. The best fit (with lowest χ^2 values) from the simulation data obtained the value of γ and δ as 0.3 and 1.76. For galaxies with velocity dispersion within $(1/8)^{th}$ of R_e (σ_8) the value of γ and δ are 0.02 and 15.92 (D13). As the disk grows around the bulge the ratio D/B increases and R_e decreases. As σ increases during compression, the ratio σ/σ_0 would grow to a value greater than one.

Since the luminosity of the bulge remains constant throughout, the decrease in effective radius would result in the surface brightness and intensity of the bulge increases. Using the definition $L \approx IR^2$, the intensity for the uncompressed classical bulge has the form:

$$I_{e,0} = I_e \left(\frac{R_e^2}{R_{e,0}^2} \right). \quad (1.17)$$

As the effective radius of the bulge decreases during the compression the ratio $\frac{R_e^2}{R_{e,0}^2}$ would become less than one, the surface brightness thus increases as the bulge is compressed.

The process of disk (re)formation around the bulge can be rapid, on the scale of few hundred million years (D13). In some of the galaxies observed as recently formed bulges, these bulges might be currently undergoing bulge compression.

Chapter 2

Sample Selection

The SDSS survey has provided many high quality observations of galaxies (York et al, 2000). The galaxies selected for this thesis were originally obtained from SDSS data release 2 (DR2) and later on these galaxies were decomposed by Gadotti (2009) (hereafter G09). This is a well studied sample of galaxies with detailed photometric data so it would not required extra decomposition work. The classification of the objects by G09 also make it more reliable and valuable for this particular study of bulge compression. The inclusion of elliptical galaxies would provide comparison to the classical bulges and the decompressed classical bulges. G09 used the two-dimensional multi-component decomposition program BUDDA (de Souza, Gadotti, & Dos Anjos, 2004) to identify the disk, bar and bulge component of each galaxy in SDSS g-, r- and i-band. Out of around 3,000 galaxies G09 selected galaxies with a number of selection criteria. The redshift range $z \leq 0.07$ was chosen to provide high enough resolution in order to identify the bars. The redshift distribution of the galaxies in fig. 2.1 showed the majority of the galaxies lie between $0.04 < z < 0.06$. The galaxies selected are not outliers from the parent population. This sample also excluded smaller galaxies (e.g. $R_e < 4''$) as the internal structures might not be decomposed properly. At this redshift of $z \leq 0.07$, the resolution of the SDSS telescope is about 1 kpc per arcsecond, which means all galaxies with $R_e \sim 1$ kpc would be resolved. The full distribution of effective radius ranges from a few hundred parsec to about 10 kpc. Classical bulges generally have $R_e < 3$ kpc while the elliptical galaxies are seldom smaller than 3 kpc. Further selection criteria rejected dwarf galaxies, low mass galaxies (stellar mass $M < 10^{10} M_\odot$), galaxies with axial ratio $b/a \leq 0.9$ (where a is the semi-major axis and b is the semi-minor axis) and galaxies with surface brightness obtained from the SDSS database. After applying the selection criteria 946 almost face-on galaxies remained. This is a small sample compared to the decomposition carried out by Simard et al (2011) for 1.12 million galaxies but the three components decomposition by G09 has provided more detailed studies of the sample than the

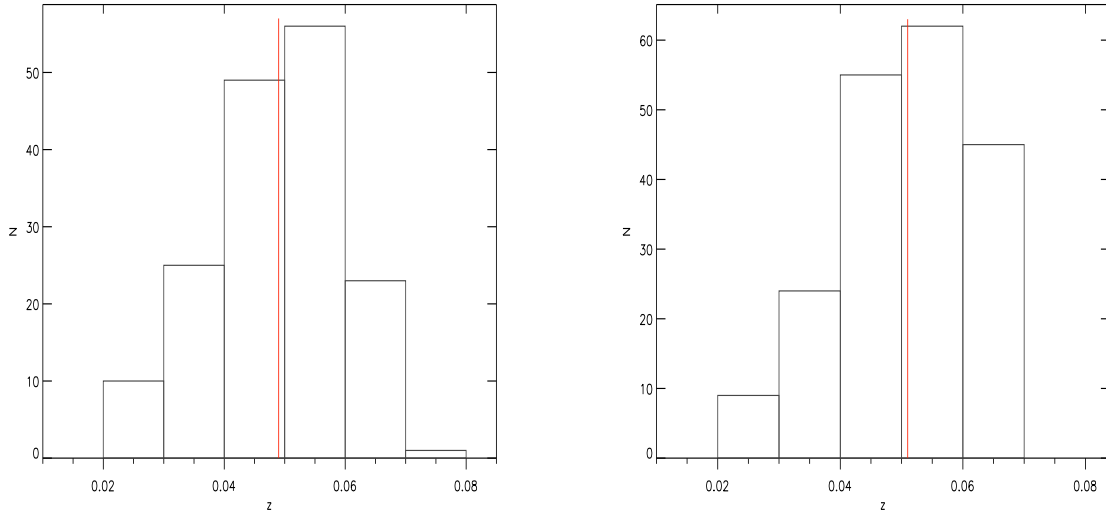


Figure 2.1: The distribution of the redshift of the classical bulges (left) and elliptical galaxies (right). The red lines represent the median redshift. The classical bulges have lower mean redshift ($z = 0.049$) compare to elliptical galaxies ($z = 0.051$).

usual two components (disk-bulge) decompositions. The original velocity dispersion from the SDSS DR2 were rejected. Instead G09 included the velocity dispersion of the objects from SDSS DR6 due to calculation bias in DR2. The error measurement becomes more on galaxies with $\sigma < 100 \text{ km s}^{-1}$. Galaxies with low σ might also include large pseudobulges.

All the graphs and numbers quoted in the following chapters are values in i-band unless otherwise specified. Two Kormendy Relations was plotted for the elliptical galaxies, barred and unbarred galaxies with $n > 2$ and $n < 2$ in fig. 8 of G09 as an indication of how the galaxies follow relations. Galaxies with $n > 2$ lie on the same Kormendy relation as elliptical galaxies. Objects with $n < 2$ have lower mean surface brightness compared to those with $n > 2$ and the latter lies at an offset from the relation. The presence of the bar does not contribute to any difference in the relations (fig. 8 of G09). The significance of $n > 2$ and $n < 2$ relate to the classification of classical bulges and pseudobulges (see chapter one). Barred galaxies have not been included in this thesis as bars can funnel gas towards the centre, leading to further star formation thus making it more difficult to compute the phenomenon of bulge decompression.

The classical bulges have been selected are those with $n > 2$. The classical bulges selected have lower mean redshift ($z = 0.049$) compared to elliptical galaxies ($z = 0.051$). The mean Sérsic index of classical bulges ($n = 3.96$) has been found to be close to elliptical galaxies ($n = 4.61$), where in both case the Sérsic index of 4 can be used to fit the light profile, which is the De Vaucouleurs profile. The normal criteria to determine bulge type via the value of bulge-to-total ratio is not valid since the galaxies was classified by G09 as elliptical

galaxies, classical bulges, pseudobulges, bulgeless and unclassified. Further limits included the rejection of negative quantities for $R_e, R_d, M_{bulge}, B/T$ on physical ground. The use of multiple selection criteria can reduce the probability of misclassifying the classical bulges. Galaxies with no velocity dispersion data from SDSS DR 6 have been rejected as velocity dispersion is essential for scaling relations and it is a parameter of the fundamental plane.

G09 provided information of velocity dispersion for 536 galaxies and has rejected galaxies with no velocity dispersion. This has reduced the sample size from 946 galaxies to 164 classical bulges and 195 elliptical galaxies. The classical bulges have been chosen in order to calculate the properties of the bulge after they have undergone bulge decompression. Pseudobulges are rejected as they might be still growing thus the change in parameters such as the effective radius and velocity dispersion might be due to the growth instead of the effect of bulge decompression.

Chapter 3

Fundamental plane

Debattista, Kazantidis, & van den Bosch (2013) carried out simulations of bulge evolution where the disk forming around the bulge. By tracing back towards the time when the bulge forms it is possible to obtain the properties of decompressed classical bulges. Comparison between the classical bulges and elliptical galaxies is then carried out with scaling relations and Fundamental Plane. Some pseudobulges do fulfill the selection criteria, but since Pseudobulges are continuously growing this can complicate the phenomenon of bulge compression. This renders them unsuitable to study for bulge compression thus they are not included in the study.

3.1 Bulge decompression

The G09 data contain three-component image decomposition for each galaxy. The velocity dispersion file provided by Gadotti (2009) (hereafter G09) contains the data for 536 galaxies while the full sample contains 946 galaxies. This project has rejected galaxies without velocity dispersion as they are necessary to compare the velocity dispersion of the bulge before and after compression as well as to compare with elliptical galaxies. The velocity dispersion of the galaxies included here are the velocity dispersion of the galaxy within $(1/8)^{th}$ of R_e (σ_8). The correction from σ to σ_8 was carried out by G09. Any future use of σ refers to the value of σ_8 . The distribution for R_e and σ for the galaxies (fig 3.1 and 3.2) have shown the decompressed classical bulges are larger than the observed classical bulges while there is a large overlapping region. The distribution of the velocity dispersions of the classical bulges and elliptical galaxies are comparable. Decompressed classical bulges have lower velocity dispersion compared to the observed classical bulges. The mean effective radius of the classical bulges has reduced from 1.39 kpc to 1.13 kpc. On average the effective radius of classical bulges decreases by 19% during compression with the maximum radius decrease of about 30% and minimum

decreases of few percents. The mean velocity dispersion has increased from 143 kms^{-1} to 151 kms^{-1} during compression. The average velocity dispersion increases by 5.9% during bulge compression.

One way to observe the effect of bulge compression is to compare the properties of the classical bulges in both decompressed and compressed (observed) state using scaling relations. $M - \sigma$ relation has been obtained for elliptical galaxies sample before comparing the result with the uncompressed classical bulges and the observed classical bulges obtained from the G09 data. Both the decompressed and observed classical bulges lie slightly above the $M - \sigma$ relation for elliptical galaxies (top of fig. 3.3). Decompressed classical bulges do not possess disks and they have been expected to behave like scaled down elliptical galaxies. The residual represents the difference between the galaxy and the relation obtained for elliptical galaxies. The relation between the mass of the bulges (and galaxies) and the residuals of the velocity dispersion (bottom of fig 3.3) agree with fig. 7 of D13 where both the decompressed and observed classical bulges lie far above the residuals for elliptical galaxies. This suggests the classical bulges follow the $M - \sigma$ relation for elliptical galaxies. The distribution for the velocity dispersion residual (fig 3.4) shows that the observed classical bulges peaked at higher values compared to the decompressed classical bulges, in agreement with fig. 8 of D13. The velocity dispersion of the classical bulges move further from the $M - \sigma$ relation for elliptical galaxies. The distribution of the residual can predict the velocity dispersion of the classical bulge increases during compression.

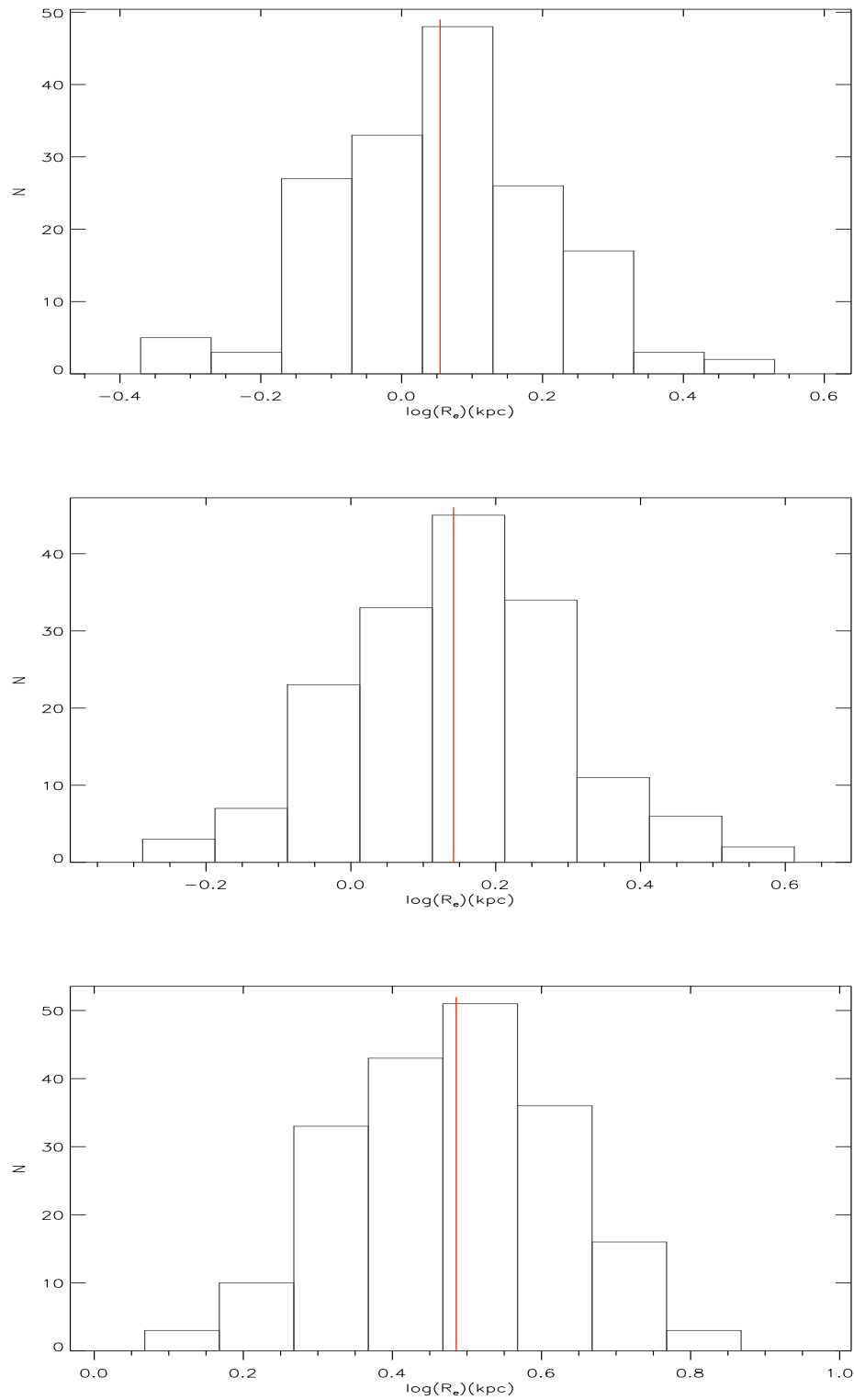


Figure 3.1: Effective radius of the galaxies of the observed classical bulges (top panel), decompressed classical bulges (middle panel) and elliptical galaxies (bottom panel). The median R_e (vertical straight line) of the observed classical bulges and decompressed classical bulges are 1.13 kpc and 1.39 kpc respectively. This shows an average decrease of 19% in R_e during compression.

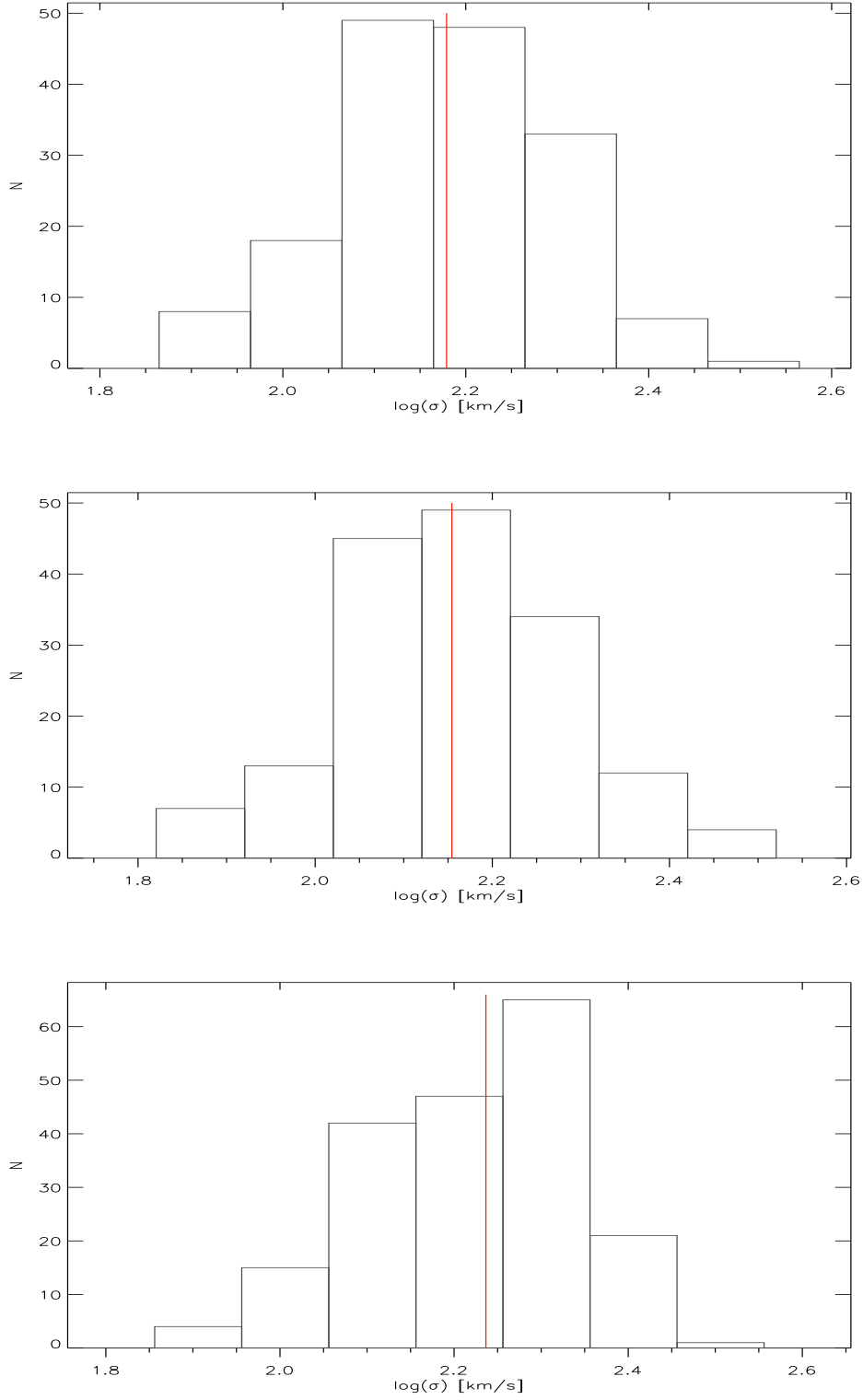


Figure 3.2: Distribution of the velocity dispersion of the galaxies with the observed classical bulges (top panel), decompressed classical bulges (middle panel) and elliptical galaxies (bottom panel). The median values of σ (vertical straight line) for the observed classical bulges and the decompressed classical bulges are 151 km/s and 143 km/s respectively. This shows an average increase of 5.9% in σ during compression.

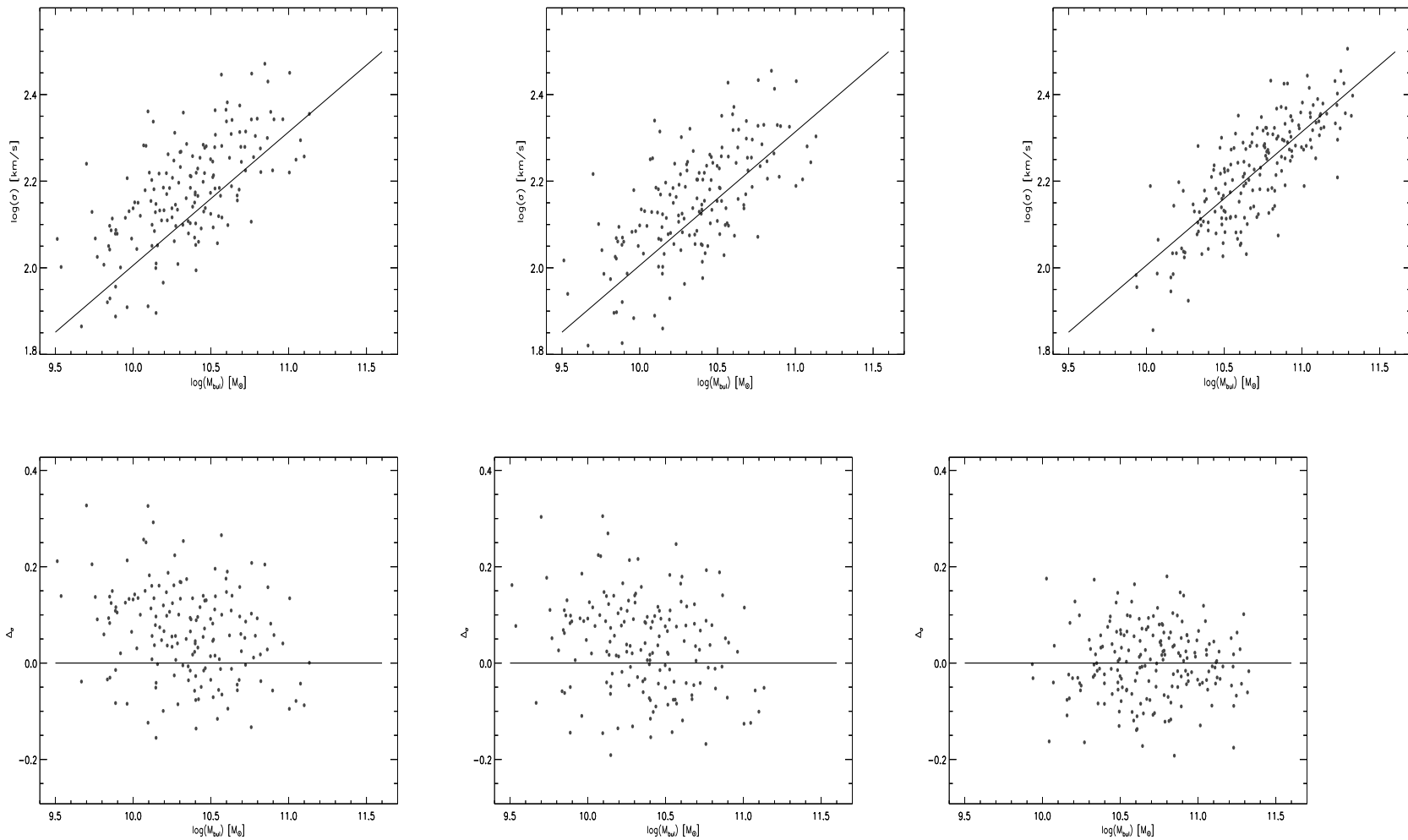


Figure 3.3: The mass-velocity dispersion relation (top panel) of the galaxies with the observed classical bulges (left), decompressed classical bulges (centre) and elliptical galaxies (right). The residuals from the $M - \sigma$ relation (bottom) have shown classical bulges are above the relation and the observed classical bulges further away from the relation.

The $R_e - \sigma$ relation (fig. 3.5) in this thesis has expanded from fig. 9 of D13 by including decompressed classical bulges (green) in order to display changes during bulge compression. As compression takes place R_e decreases and σ increases. The observed classical bulges (black) have been found at a different location to elliptical galaxies (red). Decompressed classical bulges are at an offset from both the observed classical bulges and elliptical galaxies. The effect of compression has been shown clearly for one particular classical bulge in decompressed and decompressed (observed) state (blue asterisks). However this does not mean compression would result in a straight line migration from uncompressed classical bulges to compressed classical bulges. Debattista, Kazantidis, & van den Bosch (2013) showed that the uncompressed classical bulges migrate in a curve towards the compressed (observed) classical bulges.

Surface brightness μ was included in the G09 data for different galaxy components. The surface brightness of the galaxy varies within the bulge therefore the surface brightness of the galaxy/bulge has to be converted to mean surface brightness ($\langle\mu\rangle$). Previous studies (Caon et al, 1994; Graham and Driver, 2005) found it necessary to convert μ to $\langle\mu\rangle$ as the difference between the value of μ and $\langle\mu\rangle$ increases with Sérsic index (Graham and Driver, 2005). The conversion has utilized the relation:

$$\langle\mu\rangle = \mu + 2.5 \log(2\pi/K_n) \quad (3.1)$$

where K_n is the K-correction of the object (Binney & Merrifield, 1998). This correction can be related to the Sérsic index of the object as:

$$K_n = 0.03(\log n)^2 + 0.441 \log n + 1.079. \quad (3.2)$$

Caon et al (1994) used the Sérsic index and effective radius relations ($\log n = 0.28 + 0.52 \log R_e$) previously established by Caon et al (1993). There is a second method originates from the formula to obtain the average intensity (I) within a given area (A) (e.g. $\langle I \rangle = \frac{1}{A} \int I dA$). Intensity I has been defined by the Sérsic profile ($I(R) = I_e \left(-b_n \exp \left(\frac{R}{R_e}^{1/n} - 1 \right) \right)$) (Sérsic, 1968; Graham and Colless, 1997). The mean surface brightness becomes:

$$\langle\mu_e\rangle = \mu_e - 2.5 \log \left(\frac{ne^b}{b^{2n}} \Gamma(2n) \right) \quad (3.3)$$

where $b = 2n - 0.324$ (Caon et al, 1993; Graham and Driver, 2005), which differs slightly from the relation found in G09 ($b = 2.5(0.868n - 0.142)$). The latter conversion formula has been used for this thesis. The conversion function comes from the definition of the Sérsic profile and mean intensity. Intensity(I) of the bulge/galaxy is converted to mean intensity ($\langle I \rangle$) via $\langle I \rangle = I_0 f(n)$, where $f(n) = \left(\frac{ne^b}{b^{2n}} \Gamma(2n) \right)$. The definition of the intensity of the galaxy has the form $I = b(R/R_e)^{1/n}$ where b is a factor from $f(n)$.

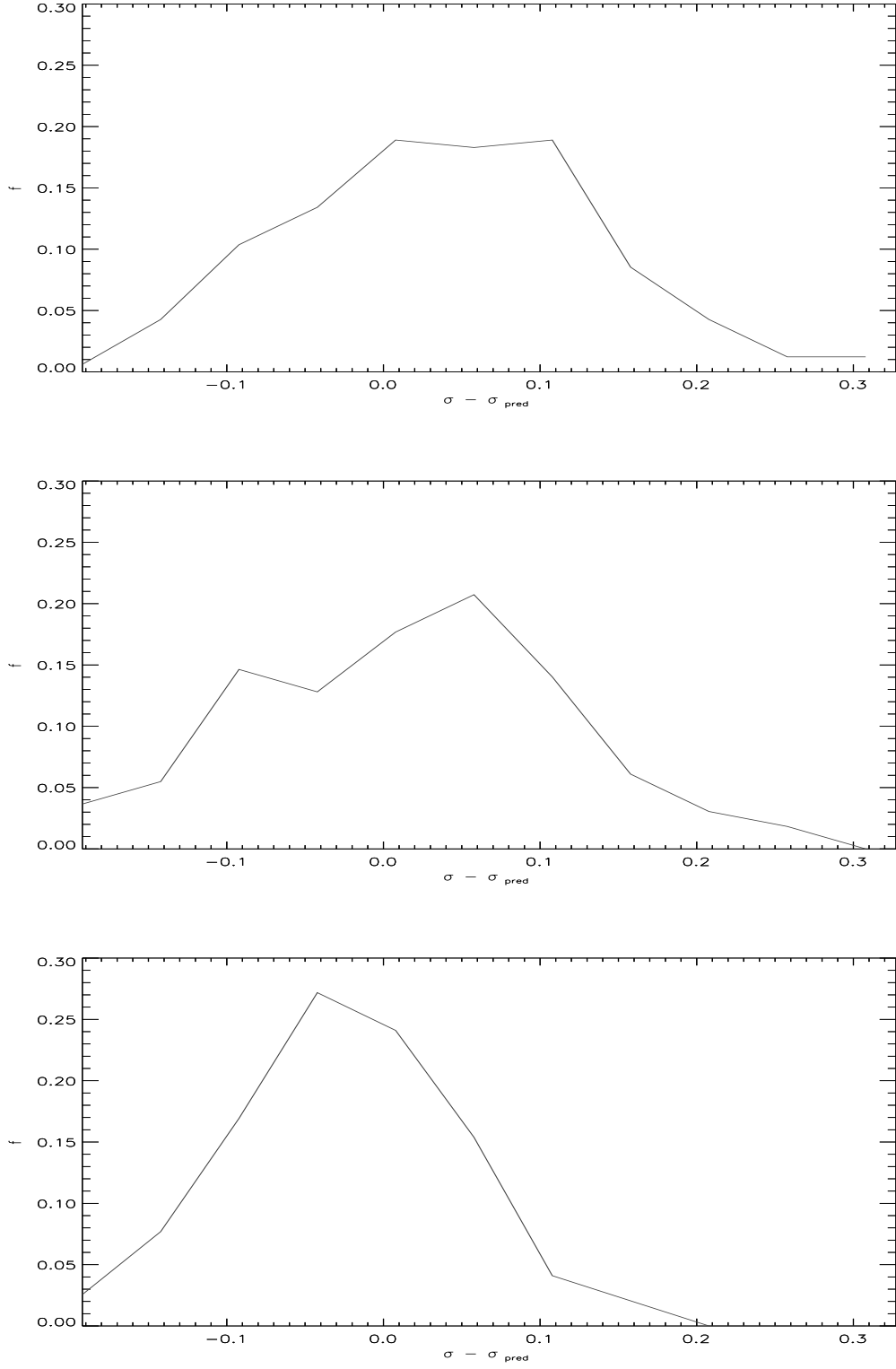


Figure 3.4: Distribution of the residuals of the $M-\sigma$ relation for observed classical bulges (top), decompressed classical bulges (middle) and elliptical galaxies (bottom)

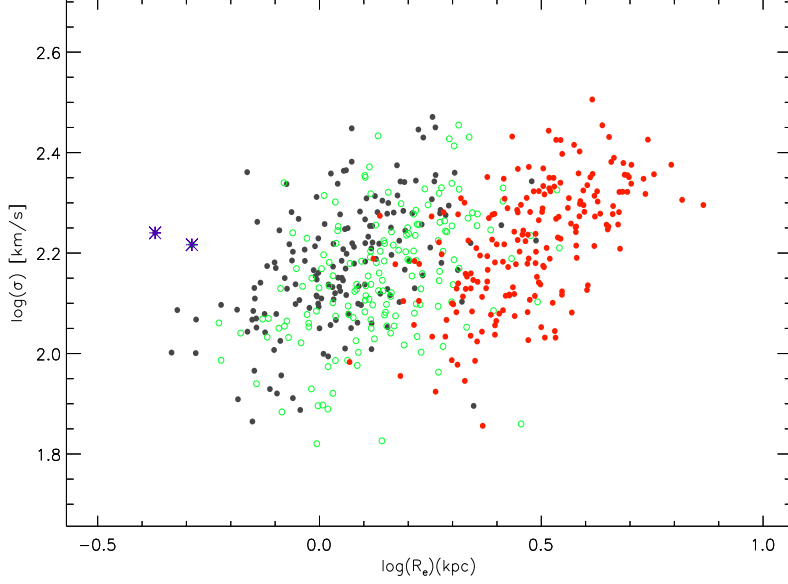


Figure 3.5: The $R_e - \sigma$ relation of the galaxies for the observed classical bulges (black), decompressed classical bulges (green) and elliptical galaxies (red). The two blue asterisks are of one chosen classical bulge in decompressed and observed state. The compression of the classical bulge can be seen from the blue asterisk on the right to the one on the left.

Both methods have provided the same mean surface brightness for galaxies. The first method allows a free Sérsic index while the latter method is more rigid due to the existence of the gamma function in the equation, which means it only allow the use of integer Sérsic indices. Since the fitting of the galaxy light profile might have non integer Sérsic index the conversion from μ to $\langle \mu \rangle$ in this thesis used the method by Caon et al (1994) with the second method as a test.

The Kormendy relation between the classical bulges and elliptical galaxies has found agreement with fig. 8 of G09 (fig. 3.6) where the observed classical bulges (black) remain on the same relation as the elliptical galaxies (red). Decompressed classical bulges (green) are found between the observed classical bulges and elliptical galaxies. The $\sigma - \langle \mu_e \rangle$ relation (fig. 3.7) has found the three groups of galaxies locate on three separate regions of the space. The blue asterisks are of a chosen classical bulge in decompressed and compressed (observed) state. The chosen classical bulge has shown small difference in surface brightness between decompressed (green) and observed (black) state. The observed classical bulges and elliptical (red) galaxies occupy two separate areas while the compressed classical bulges occupy an intermediate area between the two. The decompressed classical bulges are located between the classical bulges and elliptical galaxies. This is the same as previously seen in the Kormendy relation and $R_e - \sigma$ relation.

Another way to visualise the phenomenon of bulge decompression is to compare the bulge-to-disk size ratio

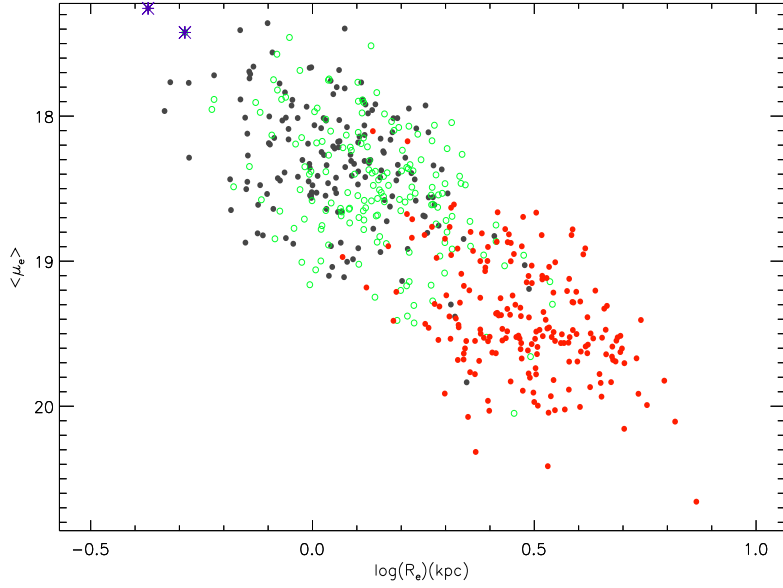


Figure 3.6: The $R_e - \langle \mu_e \rangle$ relation of the galaxies for the decompressed classical bulges (green), observed classical bulges (black) and elliptical galaxies (red). The asterisks represent one galaxy in decompressed and observed state.

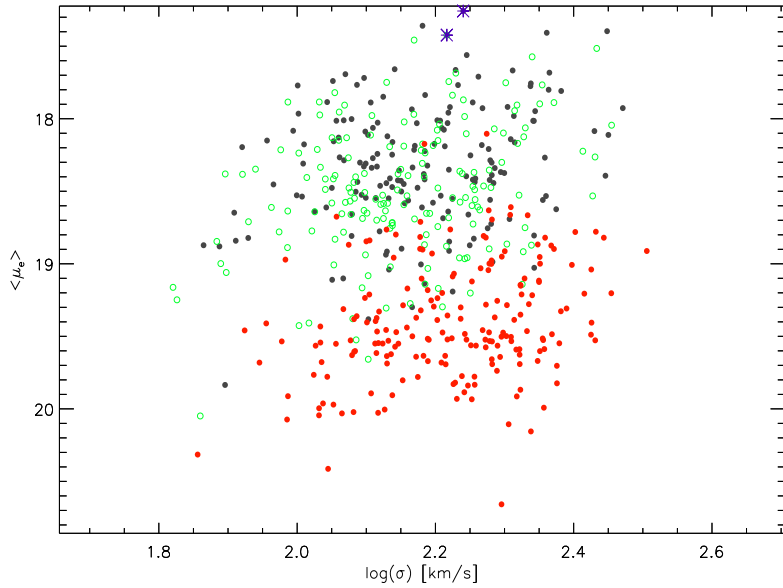


Figure 3.7: The $\sigma - \langle \mu_e \rangle$ relation of the galaxies for the decompressed classical bulges (green), observed classical bulges (black) and elliptical galaxies (red). The yellow asterisks represent one classical bulge in decompressed and observed classical state.

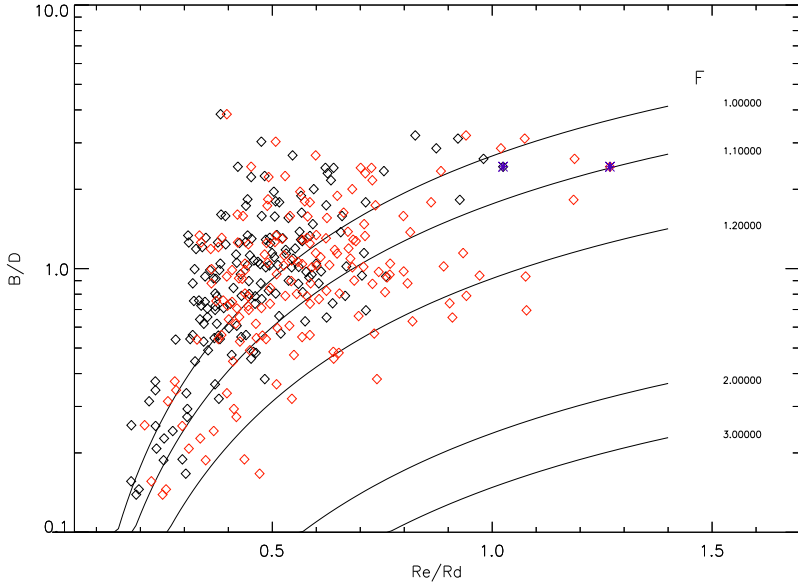


Figure 3.8: Bulge-to-disk ratio and the bulge-to-disk size ratio for observed classical bulges (black) and decompressed classical bulges (Red). One galaxy has been selected (blue asterisks) to show the evolution of the classical bulges from decompressed to observed state. The factor F is the ratio between the decompressed classical bulge velocity dispersion and observed classical bulge velocity dispersion.

and the bulge-to-disk mass ratio (D13) (fig 3.8). Galaxies in G09 are made up of bulge, disk and bars which means the fraction of bulge, disk and bars results in $(B/T) + \text{Disk } (D/T) + \text{Bar } (\text{Bar}/T) = 1$, where T is the total mass. Since the galaxies in this study are unbarred then the value $\text{Bar}/T = 0$. The value of B/D has been calculated from the data of G09 by dividing the value of B/T from the disk-to-total fraction (D/T). The value of R_e/R_d changes as bulge compression takes place, where R_e decreases and R_d increases. The values of B/D and R_e/R_d , along with equation 9 from D13 (also see eqn. 1.16 in chapter 1) have been used to calculate the growth factor (F) (black lines) for both the decompressed and observed classical bulges. The factor F is the ratio between the velocity dispersion of the decompressed classical bulges and observed classical bulges. The growth factor can then be used to obtain the photometric growth of the supermassive black hole within the host galaxy. As compression takes place galaxies migrate towards the left of the plot due to the change in R_d/R_e . This also leads to the decrease in the growth factor (blue asterisks).

3.2 Fundamental Plane fittings

The galaxies have been separated into three datasets: observed classical bulges (c), decompressed classical bulges (c_0) and elliptical galaxies (e). In order to compare the result of the Fundamental Plane with the published data this thesis has attempted to follow as closely as possible to previous studies (B03; Saulder et al, 2013). Early studies of the Fundamental Plane tended to study elliptical galaxies but later studies have also included early-type disk galaxies (Djorgovski & Davis, 1987; Jørgensen et al, 1996; Saglia et al, 2001; B03; Magoulas et al, 2012; Cappellari et al, 2013). The galaxies have been fitted for the Fundamental Plane but in order to compare with previous studies two extra datasets have been established from the current dataset: one of the observed classical bulges and elliptical galaxies (t) and another to compare whether decompression would have an effect on the fundamental plane by including decompressed classical bulges and elliptical galaxies (t_2). The Fundamental Plane fitting has been carried out for the G09 galaxies in SDSS g-, r- and i-bands. The fitting method MPFITFUN has been selected for this thesis. MPFITFUN is an add-on fitting function in *IDL* with more flexibility than the more basic LINFIT (linear fit) or MPFIT (Markwardt, 2009). MPFITFUN allows the user to input the desired formula. In order to obtain Fundamental Plane fits the formula $z = ax + by + c$ has been chosen where a, b and c are the fitted parameters of the equation while x, y and z represent the velocity dispersion, surface brightness and the effective radius of the galaxies. The fitting function obtains the parameters using a direct minimum χ^2 method where χ^2 is calculated via:

$$\chi^2 = \sum_{i=1}^n \frac{(O_i - E_i)^2}{\sigma_i^2}, \quad (3.4)$$

where n is the size of the sample, O_i is the observed variable, such as R_e of the bulge/galaxy. E_i is the expected value obtained with $ax + by + c$, where the symbols have the same meaning as above. The variable σ_i^2 is the error of the observed value. For this thesis the value of reduced χ_{red}^2 have been used. Reduced χ_{red}^2 can be found via $\chi_{red}^2 = \frac{\chi^2}{N-n-1}$, where N is the number of galaxies and n is the number of parameters fitted. MPFITFUN is one of the most robust fitting routines available where it can provide both the parameters and the error of the parameters.

The observed classical bulges have been found to stay on the Fundamental Plane with elliptical galaxies as shown in previous studies (Jørgensen et al, 1996; Falcón-Barroso et al, 2002). The Fundamental Plane is well established and the effect of compression can be seen in the change in position of the classical bulges. The Fundamental Plane can be presented with either $\log I$ or $\langle \mu_e \rangle$. This thesis has focused on the Fundamental Plane with $\langle \mu_e \rangle$ in order to avoid further conversion between $\langle \mu_e \rangle$ and $\log I$.

Fundamental Plane with $\langle \mu_e \rangle$ has shown that the decompressed classical bulges lie closer to the elliptical

galaxies (Top of fig. 3.9). As bulges compress their location on the Fundamental Plane changes, the classical bulges migrate from elliptical galaxies until compression is completed and the classical bulges are at a distance from the elliptical galaxies while still maintaining the relation. The location of the decompressed classical bulges have suggested they might be more similar to elliptical galaxies. The difference between the decompressed classical bulges and elliptical galaxies might not be of a morphological origin but instead due to the difference in the formation mechanism between classical bulges and elliptical galaxies.

The morphology of the classical bulge remains the same throughout but the inclusion of the disk affect the galaxy as a whole. Despite the changes the observed classical bulges and decompressed classical bulges are still on an approximate relation to the fitted line for the elliptical galaxies. The reason for the classical bulges to remain on the relation can be due to the influence of the disk and the bulge. As the disk grows the disk-to-bulge ratio changes but the disk is still small compare to the bulge thus the influence of the disk is still relatively small. As a result the disk galaxy is still bulge-dominated. Falc3n-Barroso et al (2002) found that bulge-dominated galaxies such as classical bulges follow the Fundamental Plane relation with elliptical galaxies. The main differences between the classical bulges are the distance of the bulges from elliptical galaxies on the Fundamental Plane and the scatter. The greater distance from elliptical galaxies is expected as the radius of the decompressed classical bulges are greater than the radius of the observed classical bulges. A further two datasets are the mixture of observed classical bulges and elliptical galaxies, and a mix of decompressed classical bulges and elliptical galaxies. They have been included for comparison with other published fundamental planes (Djorgovski & Davis, 1987; Bernardi et al, 2003; J3rgensen et al, 1996; Saglia et al, 2010). The Fundamental Plane of galaxies has confirmed that bulges, irrespective of compression, lie on the same fundamental relation as the elliptical galaxies (top of fig 3.9).

The Fundamental Plane of the classical bulges and elliptical galaxies (bottom of fig. 3.9) has provided comparison with the Fundamental Plane from other studies. The distribution for the Fundamental Plane residual agrees with the predicted properties of bulge compression as the R_e has displayed clear reduction between decompressed state (middle panel of fig. 3.10) and observed (top panel of fig. 3.10). The graphs of residuals of the Fundamental plane also shares similarity with the residuals from the $M - \sigma$ relation.

The scatter for the observed classical bulges and elliptical galaxy group, along with the decompressed observed classical bulges and elliptical galaxies group are comparable, and the scatter is greater compare to just the classical bulges, decompressed classical bulges and elliptical galaxies. The value of a obtained in this project are low compared to the values of a found in B03, D’Onofrio et al (2006) and Magoulas et al (2012). While not in complete agreement, the value of a here is comparable to the Fundamental Planes with different criteria fitted by Saulder et al (2013). The elliptical galaxies Fundamental Plane in this do not match up with the group t_1 and the group t_2 . This is understandable as the fitting process applied to all

Table 3.1: FP parameters in SDSS i-band calculated using the subroutine MPFITFUN. This table contains the Fundamental Plane fitting parameters from the classical bulges (c), elliptical galaxies (e), decompressed classical bulges (c_o), combined samples of classical bulges and elliptical galaxies (t) and combined samples of decompressed classical bulges and elliptical galaxies (t_2).

Dataset	a	b	c	Correlation Coefficient	rms	reduced χ^2
c	0.776 ± 0.065	0.215 ± 0.019	-5.570 ± 0.408	0.552	0.103	1.075
c_o	0.734 ± 0.064	0.232 ± 0.018	-5.735 ± 0.400	0.585	0.098	0.975
e	0.905 ± 0.060	0.237 ± 0.019	-6.123 ± 0.416	0.739	0.074	0.550
t	0.952 ± 0.042	0.310 ± 0.008	-7.670 ± 0.175	0.857	0.097	0.955
t_2	0.893 ± 0.041	0.274 ± 0.009	-6.837 ± 0.185	0.842	0.089	0.792

the galaxies within the dataset rather than just elliptical galaxies. The horizontal axis of the Fundamental Plane for elliptical galaxies would have different values.

3.2.1 Fundamental Plane tilting

In chapter one there was discussion about the mechanisms responsible for the deviation from the virial plane (e.g. FP tilting). The value of a obtained with the G09 galaxies deviates from two but the fittings have provided almost perfect one-to-one relation between R_e and the combination of σ and $\langle \mu_e \rangle$. The tilt in the Fundamental Plane has been thought to originate from the metallicity effect, varying IMF, varying dark matter distribution as well as deviation from homology. Due to the unavailability of data it would not be possible to investigate precisely how much each effect contributes towards the tilting of the Fundamental Plane.

Table 1 of Saulder et al (2013) demonstrated how the fitting method can affect the tilting of the fundamental Plane. The methods included the use of direct calculation, orthogonal fitting (B03; Sheth & Bernardi, 2012) and maximum likelihood (Saglia et al, 2001; Magoulas et al, 2012). Unfortunately the investigation of Fundamental Plane tilting due to different fitting methods is beyond the scope of this thesis.

3.2.2 Multi-waveband fittings

One way to observe the effect of Fundamental Plane tilting is to compare the Fundamental Plane in different wavebands. It has been found that the effect of tilting differs due to dust absorption, where the effect decreases at longer wavelength.

This thesis has utilised the data in three of the SDSS wavebands (excluding the SDSS u- and z- band) in an attempt to find the degree of Fundamental Plane tilt in different wavebands. The availability of only three wavebands means the comparison may be less profound compared to the Fundamental Plane study in Saulder et al (2013). When comparing the observed classical bulges with the decompressed

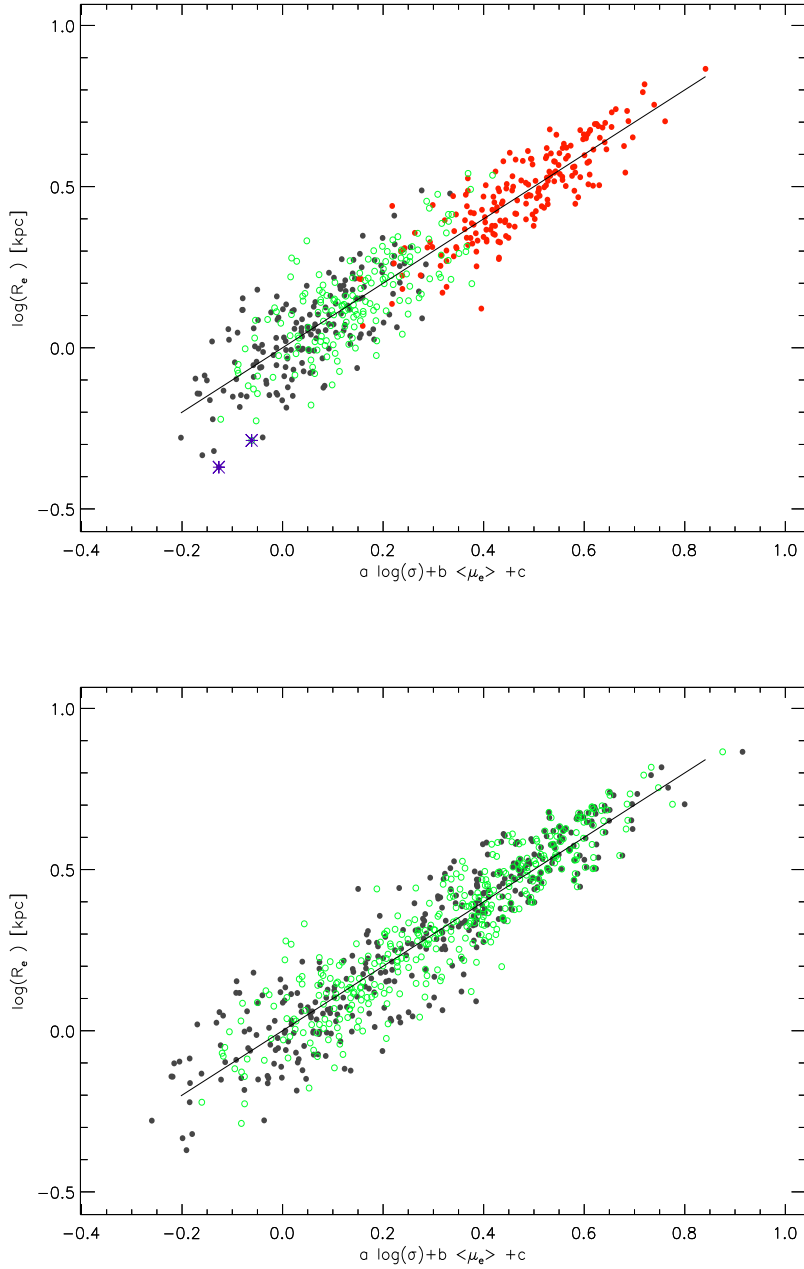


Figure 3.9: Edge-on view of the fundamental plane ($R_e - \sigma - \langle \mu_e \rangle$) obtained using the IDL subroutine MPFITFUN. Top panel: The Fundamental Plane for elliptical galaxies (red), observed classical bulges (black) and decompressed classical bulges (green). Bottom panel: Edge-on view of the fundamental plane for two groups of galaxies: the group incorporating observed classical bulges and elliptical galaxies (black) and the group incorporating of decompressed classical bulges and elliptical galaxies (green).

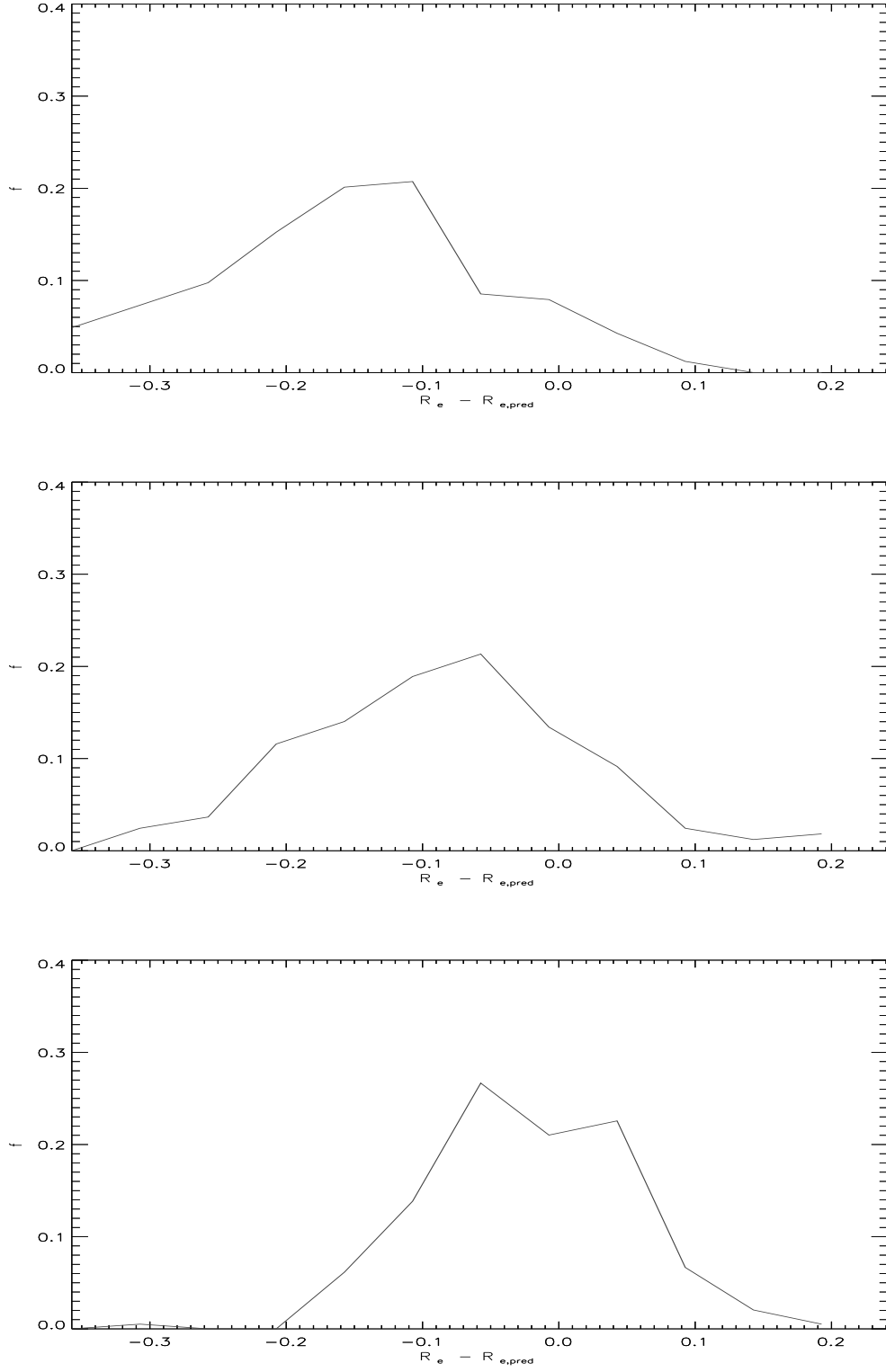


Figure 3.10: Distribution of the residuals of the Fundamental Plane for observed classical bulges (top), decompressed classical bulges (middle) and elliptical galaxies (bottom)

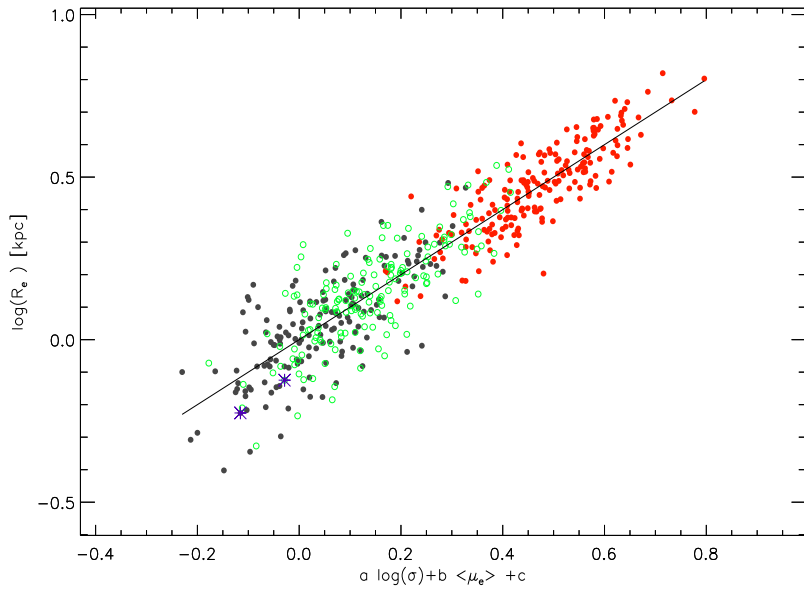
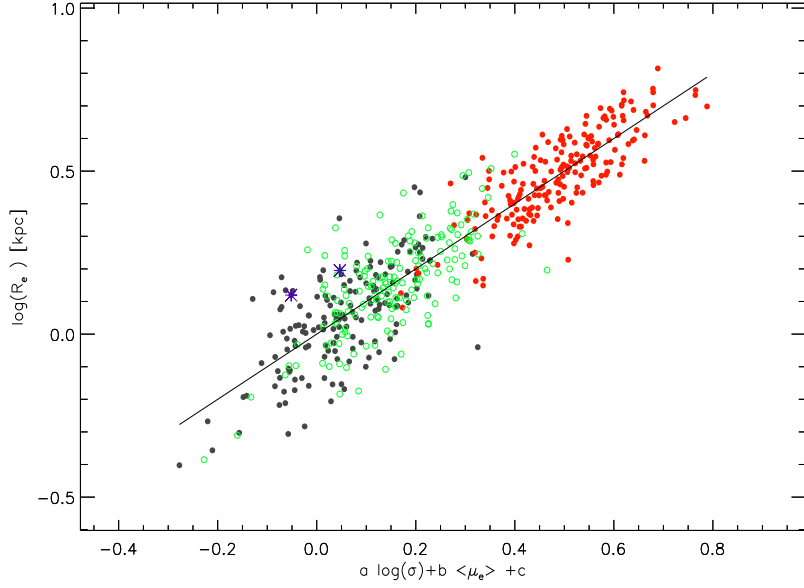


Figure 3.11: Edge-on view of the Fundamental Plane ($R_e - \sigma - \langle \mu_e \rangle$) in SDSS g- and r- band for the observed classical bulges (black), decompressed classical bulges (green) and elliptical galaxies (red).

Table 3.2: The edge-on view of the fundamental plane in SDSS g- and r-band. This table contains the Fundamental Plane fitting parameters, correlation coefficient, root mean square error and χ^2 error for the classical bulges (c), elliptical galaxies(e), decompressed classical bulges (c_o), combined samples of classical bulges and elliptical galaxies (t) and combined samples of decompressed classical bulges and elliptical galaxies (t_2)

Dataset	a	b	c	Correlation Coefficient	rms	reduced χ^2
g-band						
c	0.720 ± 0.064	0.182 ± 0.017	-5.095 ± 0.394	0.475	0.114	1.308
c_o	0.671 ± 0.063	0.203 ± 0.016	-5.330 ± 0.387	0.526	0.106	1.144
e	0.779 ± 0.059	0.210 ± 0.018	-5.613 ± 0.420	0.683	0.078	0.609
t	0.893 ± 0.042	0.305 ± 0.008	-7.864 ± 0.183	0.813	0.113	1.279
t_2	0.839 ± 0.040	0.264 ± 0.008	-6.875 ± 0.194	0.802	0.098	0.969
r-band						
c	0.826 ± 0.066	0.212 ± 0.018	-5.718 ± 0.405	0.554	0.105	1.120
c_o	0.777 ± 0.065	0.229 ± 0.017	-5.869 ± 0.399	0.585	0.100	1.019
e	0.862 ± 0.060	0.227 ± 0.019	-5.949 ± 0.435	0.716	0.074	0.552
t	0.968 ± 0.042	0.306 ± 0.008	-7.768 ± 0.180	0.850	0.099	0.992
t_2	0.900 ± 0.041	0.270 ± 0.009	-6.889 ± 0.189	0.836	0.090	0.808

classical bulges one matter of concern is whether the compression of classical bulges provide better fitting parameters. The quality of the Fundamental Plane in i-band can be determined by comparing the reduced χ^2 values, the root mean square coefficient and the correlation coefficient. Irrespective of wavebands the group incorporates decompressed classical bulges and elliptical galaxies have lower reduced χ^2 values, lower root mean square coefficient and higher correlation coefficient compared to the group with observed classical bulges and elliptical galaxies (fig. 3.11). The value of a on the whole is lower ($a = 0.952$) than the value of a in B03 ($a = 1.52$). A later study (Saulder et al, 2013), using SDSS DR 8 data, found the value of a ($a = 1.075$) comparable to the value in this thesis. In B03 and Saulder et al (2013) the effect of Fundamental Plane tilting decreases towards shorter wavebands. The trend has not been seen for the observed classical bulges or decompressed classical bulges (see table 3.2). This trend has been observed in elliptical galaxies, the value of a has increased from 0.779 in g-band to 0.905 in i-band. The inclusion of classical bulges in any group of galaxies results in the increase in a when observed in g- to r-band but not in i-band. The Fundamental Planes in g- and r-bands have also found to have a similar trend during compression: classical bulges migrate away from elliptical galaxies while remaining on the Fundamental Plane relations for elliptical galaxies (fig 3.11). The observational waveband has no visible effect on the shape of the Fundamental Plane.

Chapter 4

Conclusion and Summary

With a sample of processed galaxies from Gadotti (2009), this thesis has studied the effect of bulge compression by obtaining physical parameters R_e and σ for the decompressed classical bulges. This thesis has also determined this effect by using scaling relations and the Fundamental Plane. In order to compare the difference between the observed and decompressed classical bulges a number of scaling relations such as the Kormendy, $R_e - \sigma$, $\sigma - \langle \mu_e \rangle$ relation has been used. Such relations have previously been used by Gadotti (2009) and Debattista, Kazantidis, & van den Bosch (2013).

Both unbarred disk galaxies and elliptical galaxies have been included in this study. The effect of bulge compression, instead of being observed in terms of the change of the Sérsic index as in Andreadakis (1998), was derived as a change in the bulge physical properties, following Debattista, Kazantidis, & van den Bosch (2013). Adiabatic compression in classical bulges happens when a disk forms around a bulge. The effect of bulge compression can be observed as a decrease in the size of the bulge and an increase in the velocity dispersion of the bulge, with the assumption that the mass and luminosity of the bulge remains constant during compression. This along with the simulated data by Debattista, Kazantidis, & van den Bosch (2013) have obtained the effective radius, velocity dispersion and the surface brightness of the decompressed classical bulges.

The effect of decompression can be seen when comparing the position of the classical bulges along with the elliptical galaxies on the Fundamental Plane. The decompressed classical bulges also follow the scaling relations and are found between the observed classical bulges and elliptical galaxies. Fundamental Plane fittings have found classical bulges migrate from elliptical galaxies during compression. Similar results have been obtained for the classical bulges in the Kormendy relation.

Observational wavebands have been found to affect the tilting of the Fundamental Plane (Saulder et al,

2013) although in this thesis it holds true only for elliptical galaxies but not for either decompressed classical bulges or observed classical bulges.

The combination of the observed classical bulges and elliptical galaxies has provided a dataset similar to that of the studies fitting the Fundamental Plane for E/S0 galaxies. The Fundamental Plane has suffered greater tilting compared to other SDSS Fundamental Plane studies (Bernardi et al, 2003; Díaz & Muriel, 2005; Saulder et al, 2013). The comparison between the group consists of observed classical bulge and elliptical galaxies with the group consists of decompressed classical bulge and elliptical galaxies have found that the former have higher correlation coefficients and have a value of reduced χ^2 closer to one, the latter have marginally lower rms error. The fact that the decompressed classical bulges lie on the same relation means that they must share some similarity. On the other hand the difference between the decompressed classical bulges and elliptical galaxies on the scaling relations and the Fundamental Plane suggest that this might possibly be due to the difference in the formation history between classical bulges and elliptical galaxies.

Bibliography

- Abazajian K. et al. 2009,*ApJS*, 182,543
- Aceves H., & Velázquez H. 2005,*MNRAS*, 360,L50
- Andreadakis Y.C. 1998,*MNRAS*, 267,283
- Andreadakis Y.C., & anders R. H. 1995,*MNRAS*, 267, 283
- Athanassoula E. 2005,*MNRAS*, 358,1477
- Bender R., Burstein D., & Faber S.M. 1992,*ApJ*, 399,462
- Bernardi M. et al 2003,*ApJ*, 125,1881
- Binney J., & Merrifield M. 1998,*Galactic Astronomy*, Princeton,ISBN:978-0-691-02565-0
- Blumenthal G. R., Faber S. M., Flores R., & Prinnack J. R. 1986,*ApJ*, 301, 27
- Bolton A. S., Burles S., Treu T., Koopmans L. V. E., & Moustakas L. A. 2007,*ApJ*, 665,L108
- Boylan-Kolchin M., Ma C. P.,& Quataert E. 2005,*MNRAS*, 362, 184
- Caon N., Capaccioli M.,& D'Onofrio M. 1993,*MNRAS*, 265,1013
- Caon N., Capaccioli M., D'Onofrio M.,& Longo G. 1994,*A & A*, 286,L39
- Cappellari M., Scott N., Alatalo K., Blitz L., Bois M., Bournaud F., Bureau M., Crocker A. F., Davies R. L., Davis T. A., de Zeeuw P. T., Duc P., Emsellem E., Khochfar S., Krajnović D., Kuntschner H., McDermid R. M., Morganti R., Naab T., Oosterloo T., Sarzi M., Serra P., & Weijmans A.,2013,*MNRAS* , 432,1709
- Capelato H. V., de Carvalho R. R., & Carlberg R. G. 1995,*ApJ*, 451, 525
- Cardone V. F., & Sereno M. 2005,*A & A*, 438, 545
- Ceverino D., Dekel A., Tweed D., & Primack J. 2015,*MNRAS*, 447, 3291

Cheung E., Athanassoula E., Masters K. L., Nichol R. C., Bosma A., Bell E. F., Faber S. M., Koo D. C., Lintott C., Melvin T., Schawinski K., Skibba R. A., & Willett K. W. 2013, *ApJ*, 779,162

Ciotti L. 1991, *A & A*, 249,99

Ciotti L., Lanzoni B., & Renzini A., 1996, *MNRAS*, 282,1

D’Onofrio M., Valentinuzzi T., Secco L., Caimmi C., & Bindoni D. 2006, *New Astronomy Reviews*, 50,447

D’Onofrio M., Fasano G., Moretti A., Marziani P., Bindoni D., Fritz J., Varela J., Betoni D., Cava A., Poggaiani B., Gullieuszik M., Kjærgaard P., Moles M., Vulcani B., Omizzolo A., Couch W. J., & Dressler A. 2013, *MNRAS*, 435,45

de Vaucouleurs G. 1948, *AnAp*, 11, 247

Debattista V.P, Kazantidis S., & van den Bosch F. C. 2013, *ApJ*, 765, 23

de Souza R. E., Gadotti D. A., & Dos Anjos S. 2004, *ApJS*, 153, 411

Díaz E., & Muriel H. 2005, *MNRAS*, 364, 1299

Djorgovski S. & Davis M. 1987, *ApJ*, 313,59

Dressler A., Lynden-Bell D., Burstein D., Davies R. L., Faber S. ., Terlevich R. J., & Wegner G. 1987, *ApJ*, 313,42

Dutton A. A., Macciò A. V., Trevor Mendel J., & Simard L. 2013, *MNRAS*, 432,2496

Eggen O.J., Lynden-Bell D., & Sandage A.R. 1962, *ApJ*, 136,748

Faber S.M. & Jackson R.E. 1976, *ApJ*, 204,668

Falcón-Barroso J., Peletier R.F., & Balcells M. 2002, *MNRAS*, 335,741

Ferrarese L., & Merritt D. 2008, *ApJ*, 539, L9

Fisher D.B., & Drory N. 2008, *AJ*, 136,773

Fisher D.B., & Drory N. 2010, *ApJ*, 716,969

Fernández Lorenzo M., Cepa J., Bongiovanni A., Pérez García A. M., Ederoclite A., Lara-López M. A., Pović M., Sánchez-Portal M. 2011, *A&A*, 526,A72

Fraix-Burnet D., Dugué M., Chattopadhyay T., Chattopadhyay A. K., & Davoust E. 2010, *MNRAS*, 407,2207

Fraix-Burnet D. 2011, *MNRAS*, 416, L36

Galaz G., Villalobos A., & Infante L. 2006, *ApJ*, 131, 2035

Gadotti D. 2008, *MNRAS*, 384, 420

Gadotti D. 2009, *MNRAS*, 393, 1531

Gadotti D., & Kauffmann G. 2009, *MNRAS*, 399, 621

Graham A. W., & Colless M. 1997, *MNRAS*, 287, 221

Graham A. W., & Driver. 2005, *PASA*, 22, 118

Guedes J., Mayer L., Carollo M., & Madau P. 2013, *ApJ*, 772, 36

Hartmann M., Debattista V. P., Cole D. R., Valluri M., Widrow L. M., & Shen J. 2014, *MNRAS*, 441, 1243

Herbert P.D., Jarvis M. J., Willot C. J., McLure R. J., Mitchell W., Tawlings S., Hill G. J., & Dunlop J. S. 2011, *MNRAS*, 410, 1360

Hjorth J., & Madsen J. 1995, *ApJ*, 445, 55

Hyde J.B. & Bernardi M. 2009, *MNRAS*, 396, 1171

Immeli A., Samland M., Gerhard O., & Westera P. 2004, *A&A*, 413, 547

Jeset R., Naab T., & Barkert A. 2002, *ApJ*, 571, 289

Jørgensen I., Franx M. & Kjørgaard 1996, *MNRAS*, 280, 167 ADD INITIAL

Keselman J. A., & Nusser A. 2012, *MNRAS*, 424, 1232

Kormendy J. 1977, *ApJ*, 218, 333

Kormendy J. 1985, *ApJ*, 295, 73

Kormendy J. & Kennicutt Kr. C. 2004, *ARAA*, 42, 403

Lintott C., Schawinski K., Bamford S., Slosar A., Land K., Thomas D., Edmondson E., Masters K., Nichol R. C., Raddick M. J., Szalay A., Andreescu D., Murray P., & Vandenberg J. 2011, *MNRAS*, 420, 166

MacArthur L.A., Ellis R.S., Treu T., & Moran S.M. 2010, *ApJL*, 709, L53

Magoulas C., Springob M., Colless M., Jones D. H., Campbell L. A., Lucey J. R., Mould J., Jarrett T., Merson A., & Brough S. 2012, *MNRAS*, 427, 245

Markwardt C. B. 2009, *ASPC*, 411, 251

Masters K. L., Nichol R. C., Hoyle B., Lintott C., Bamford S. P., Edmondson E. M., Forston L., Keel W. C., Schawinski K., Smith A. M., & Thomas D. 2011, *MNRAS*, 411, 2026

Méndez-Abreu., Debattista V.P., Corsini E.M., & Aguerri J.A.L 2014, *A&A*, 572, A22

Mo H., van den Bosch F., & White S. 2011, *Galaxy Formation and Evolution*, Cambridge, ISBN:978-0-521-85793-2

Mollá M., & Ferrini F. 1995, *ApJ*, 454, 726

Okamoto T. 2013, *MNRAS*, 428, 718

Pahre M.A., Djorgovski S.G., & de Carvalho R.R., 1995, *ApJ*, 453, L17

Prugniel Ph., & Simien F. 1997, *A & A*, 321, 111

Saglia R. P., Sánchez-Blázquez, Bender R., Simard L., Desai V., Aragón-Salamanca A., Milvang-Jensen B., Halliday C., Jablonka P. Noll S., Poggianti B., Clowe D. I., De Lucia G., Pelló R., Rudnick G., Valentinuzzi T., White S. D. M., & Zaritsky D. 2001, *A & A*, 524, A6

Saglia R. P., Sánchez-Blázquez P., Bender R., Simard L., Desai V., Aragón-Salamanca A., Milvang-Jensen B., Halliday C., Jablonka P., Noll S., Poggianti B., Clowe D. I., De Lucia G., Pelló R., Rudnick G., Valentinuzzi T., White S. D. M., & Zaritsky D. 2010, *A & A*, 524, A6

Saulder C., Mieske S., Zeilinger W.W., & Chilingarian I. 2013, *A&A*, 557, A21

Sellwood J. A., & McGaugh S. S. 2005, *ApJ*, 634, 76

[Sérsic J. L. 1968, *Atlas de galaxias australes (Cordoba, Argentina: Observatorio Astronomico, 1968)*

Sheth R.K., & Bernardi M. 2012, *MNRAS*, 422, 1825

Simard L., Mendel J. T., Patton D. R., Ellison S. L., & McConnachie A. W. 2011, *ApJS*, 196, 11

Trujillo I., Burkert A., & Bell E.F. 2004, *ApJ*, 600, L39

van de Sande J., Kriek M., Franx M., Bezanson R., & van Dokkum P.G. 2014, *ApJ*, 793, L31

van den Bosch 1998, *ApJ*, 507, 601

van Dokkum P.G. & Franx M. 1996 *MNRAS*, 281, 985

van Dokkum P.G. & Stanford S.A. 2003*ApJ*, 585,78

Wolf J., Martinez G. D., Bullock J. S et al 2010,*MNRAS*, 406, 1220

York D. G. et al. 2000,*AJ*, 120, 1579